Geology of Ore Deposits, Vol. 46, No. 6, 2004, pp. 409–440. Translated from Geologiya Rudnykh Mestorozhdenii, Vol. 46, No. 6, 2004, pp. 475–509.
Original Russian Text Copyright © 2004 by Bortnikov, Bryzgalov, Krivitskaya, Prokof'ev, Vikentieva.
English Translation Copyright © 2004 by MAIK "Nauka/Interperiodica" (Russia).

The Maiskoe Multimegastage Disseminated Gold–Sulfide Deposit (Chukotka, Russia): Mineralogy, Fluid Inclusions, Stable Isotopes (O and S), History, and Conditions of Formation

N. S. Bortnikov*[1], I. A. Bryzgalov, N. N. Krivitskaya**, V. Yu. Prokof'ev**, and O. V. Vikentieva****

**Institute of Geology of Ore Deposits, Petrography, Mineralogy, and Geochemistry (IGEM), Russian Academy of Sciences, Staromonetnyi per. 35, Moscow, 119017 Russia*
***Moscow State University, Vorob'evy gory, Moscow, 119992 Russia*
Received October 15, 2003

Abstract—A study of the sequence and stages of the mineral-forming processes, chemical compositions of sulfides, fluid inclusions, and sulfur isotopes in sulfides and oxygen isotopes in quartz of the Maiskoe deposit has been carried out. Three genetically different mineralization styles of various ages, which were formed in different geological and tectonic environments, have been superimposed at the Maiskoe deposit. Disseminated auriferous pyrite–arsenopyrite ores formed during the early gold–sulfide stage. Different mineral aggregates composing cassiterite–sulfide veins originated during the next rare metal stage. Quartz–stibnite veins formed during the final gold-stibnite stage. The following two types of fluid inclusions were found in quartz from different mineralization zones: (1) three-phase inclusions containing liquid, a vapor bubble (with liquid CO_2), and solid (halite, rarely two or three soluble phases); (2) three-phase inclusions containing liquid, a vapor bubble (without liquid CO_2), and solid (halite); (3) three-phase H_2O-rich inclusions with liquid CO_2; (4) three-phase vapor-rich inclusions; and (5) two-phase inclusions containing liquid and a vapor bubble. Three fluids of different compositions and physicochemical parameters are assumed to have been involved in the ore-forming system of the deposit. A $H_2O + CO_2 + CH_4$ fluid with a salt content of 8.2–2.2 wt % NaCl-equiv. deposited the economically valuable auriferous sulfide ores at 360–240°C and 1.1–0.9 kbars. A highly saline (37.5–30.0 wt % NaCl-equiv.) fluid and a low saline fluid formed the cassiterite–sulfide ores, which crystallized at a temperature of 500–170°C. The quartz–stibnite ores precipitated from an aqueous fluid with a salinity of 10.1–0.7 wt % NaCl-equiv. at 250–120°C. The $\delta^{34}S$ values for arsenopyrite and pyrite from the auriferous orebodies range from –6.9 to –0.6 and –1.1 to –8.8‰, respectively. The $\delta^{34}S$ values in sulfides from the cassiterite–sulfide mineralization are from –5.9 to –7.6 ‰ for pyrite, –1.8 to +4.1‰ for sphalerite, –0.4 to –7.9‰ for galena, and –4.9 to –6.1‰ for sulfosalt minerals. The $\delta^{34}S$ values for stibnite vary from –9.9 to +0.8‰. The $\delta^{18}O$ values of quartz from auriferous zones are from +11.8 to +14.5‰, those of quartz from the veins formed during the cassiterite–sulfide megastage are from +1.7 to +4.1‰, and those of quartz from the quartz–stibnite veins are from +12.2 to +15.2‰. The ore formation conditions are assumed to have changed from mesoabyssal (the auriferous sulfide megastage) through shallow depth (the rare metal megastage) to subsurficial (the gold–stibnite megastage) environments. Fluids of magmatic origin and fluids originated at the heating of meteoric waters penetrated the hydrothermal system. The role of the latter fluids increased toward later megastages of this hydrothermal system.

INTRODUCTION

Numerous gold deposits are known within accretionary-fold belts in the northeastern territory of Russia. The Nezhdaninskoe, Natalkinskoe, and Maiskoe deposits, which are of great economic importance, are among them. The accretionary-fold belts in the northeastern territory of Russia formed during the Cenozoic to Mesozoic eras as a result of an interaction of the Siberian paleocontinent with Pacific oceanic plates (Parfenov *et al.*, 1993; Parfenov, 1995; Shpikerman, 1998; Shpikerman and Goryachev, 1996). The accretionary structure of northeastern Asia consists of terranes of different origin amalgamated to the craton during a long time (Parfenov *et al.*, 1993). A very important role in the territory development was played by the tectonomagmatic activization related to the formation of the Chukotsk–Okhotsk volcanoplutonic belt. As a result, a spatial superposition of mineralizations of different styles was suggested in many ore districts and fields in the northeastern territory of Russia.

The Maiskoe disseminated gold–sulfide deposit, which consists of orebodies with superimposed mineralizations of different styles (Volkov and Sidorov, 2001; Novozhilov and Gavrilov, 1999), is among such deposits. It is situated in the Chukotsk national district 150 km southeast of Pevek harbor (Fig. 1). The deposit was discovered in 1972 as the result of reexploration of an antimony occurrence (Novozhilov and Gavrilov,

[1]Corresponding author: N.S. Bortnikov. E-mail: bns@igem.ru

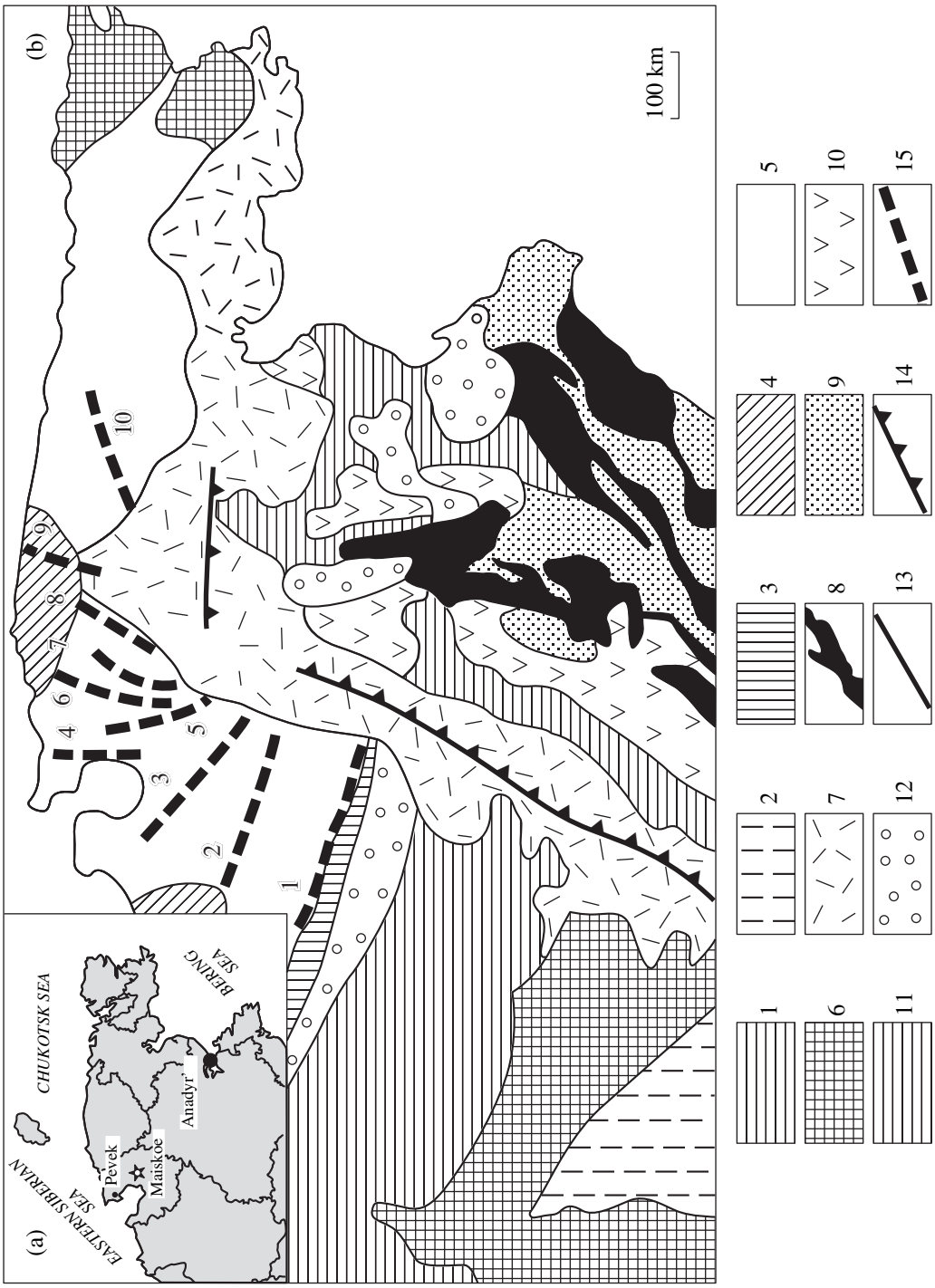
(a)
EASTERN SIBERIAN SEA
CHUKOTSK SEA
BERING SEA
Pevek
Maiskoe
Anadyr'
(b)
100 km
1
2
3
4
5
6
7
8
9
10
1
2
3
4
5
6
7
8
9
10
11
12
13
14
15

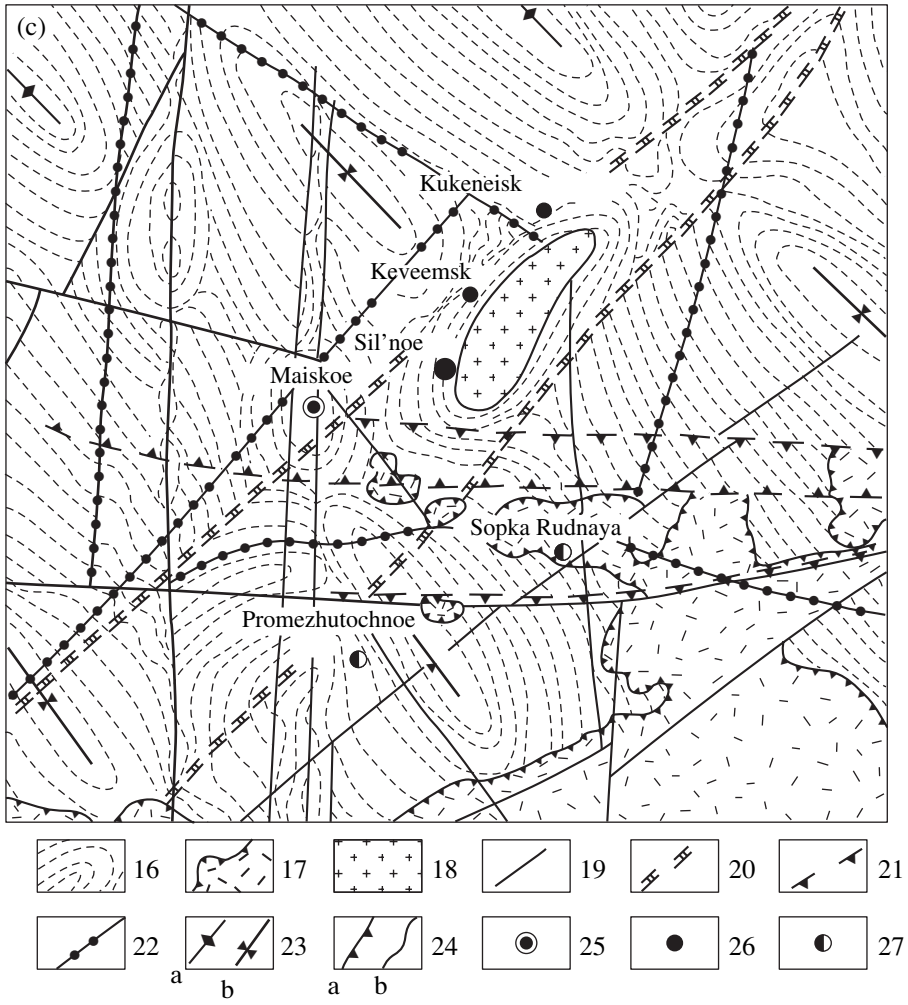

Fig. 1. (Contd.)

1999). The average gold grade is 12 g/t (Konstantinov *et al.*, 2000). The geological structure, tectonics, magmatism, and metallogeny of the region have been studied in detail by many researchers (Shilo *et al.*, 1988; Novozhilov and Gavrilov, 1999; Sidorov and Volkov, 2001; Volkov and Sidorov, 2001). There is no consensus on the sequence and stages of the mineral-forming processes. This leads to contradictive interpretation of the deposit origin.

Most researchers suggest that the Maiskoe deposit was formed during two megastages of a mineral-forming process, such as early rare metal and late auriferous ones (Novozhilov *et al.*, 1982; Konstantinov *et al.*, 2000). Tomson *et al.* (1984) believed that finely dis-

Fig. 1. Scheme of location of the Maiskoe deposit (a), tectonic structure of the northeast of Russia (b), and geological setting of the Kukeneisk intrusive–cupola structure (Maiskii ore district) (c) (Sidorov and Volkov, 2001). 1—Fragments of Alazeisk and Oloisk riftogenous zones; 2—fragments of Ol'dzhoisk and Sugoisk fold zones created on a thinned continental crust; 3—Yuzhno-Anyuisk collision zone; 4, 5—Chukotsk system: 4—uplifts of Paleozoic rocks, 5—Mesozoic orogenic structures; 6—fragments of pre-Riphean continental crust; 7—Okhotsk–Chukotsk volcanic belt; 8—zones and blocks with ophiolite allochthones; 9—fold belts of the Koryak Highland composed of Cretaceous flysch–olistostrome sequences; 10—Cenozoic volcanic belts and fields; 11—Udsk–Murgal'sk island arc system; 12—Neogene–Quaternary depression; 13—nondifferentiated faults; 14—boundary of interior and outer zones of the Okhotsk–Chukotsk belt; 15—ore-bearing zones of tectonomagmatic activization: 1—Yuzhno-Anyuisk, 2—Keperveemsk, 3—El'veneisk, 4—Val'kumeisk, 5—Palyansk, 6—Karpungsk, 7—Kukeneisk, 8—Matenvunaisk, 9—Pinkhinkuul'–Ryveemsk, 10—Ekugsk; 16—Middle to Early Triassic terrigenous flysch sequence; 17—Early Cretaceous volcanics; 18—Early to Late Cretaceous granites; 19—faults; 20—northeast-trending subvolcanic faults; 21—neotectonic faults; 22—faults inferred from geophysical data; 23—anticline (a) and syncline (b) fold axes; 24—boundaries of volcanic rocks of the Okhotsk–Chukotsk volcano–plutonic belt (a) and geological boundaries (b); 25–27—ore deposits: 25—gold–sulfide, 26—cassiterite–sulfide, 27—gold–stibnite.

seminated pyrite and arsenopyrite, bearing "invisible" gold, formed before quartz veins and veinlets. Volkov (1995) recognized four megastages: (1) metamorphogenic quartz, (2) rare metal, (3) auriferous, and (4) antimony. These suggestions did not essentially change in later publications of these authors (Novozhilov and Gavrilov, 1999; Volkov and Sidorov, 2001). However, it was inferred that the quartz–stibnite association was formed during a separate third megastage. Interpretations of mineral formation stages during these megastages by the above-cited researchers are different as well.

One of the questions that should be answered is whether different ores located in a district with a complicated history of geodynamic development result from the hydrothermal activity related to one or several tectonomagmatic pulses. The study of the origin, chemistry, and evolution of mineral-forming fluids can help to solve this problem.

The origin of gold deposits hosted by terrigenous, siltstone-carbonaceous, and carbonaceous (black shale) sequences is a debatable problem as well. There is no consensus on the genesis of lode gold–quartz deposits and disseminated gold deposits. One group of researchers referred them to different genetic styles, while other researchers considered them as genetically related deposits (Bierlein and Maher, 2001). Different points of view on their origin (hydrothermally exhalative, orthomagmatic, and metamorphic) were suggested (Sidorov and Tomson, 2000; Buryak *et al.*, 1990; Kurbanov *et al.*, 1994; Hodgson *et al.*, 1993). American geologists offered a hypothesis on the predominant role in their formation of metamorphic fluids (Goldfarb *et al.*, 1989). A convective-meteoric hypothesis for the origin of North Cordilleran deposits has been proposed (Nesbitt and Muchlenbachs, 1989). During the last five years, American geologists developed concepts that some gold deposits in Alaska are related to I-granites and occur in the districts where tin- and tungsten-bearing granites are spread (Newberry *et al.*, 1995; McCoy *et al.*, 1997; Thompson and Newberry, 2000).

This paper present results of a comprehensive study of mineral compositions of ores, chemical compositions of minerals, the depositional sequence of different mineral aggregates, fluid inclusions, and sulfur and oxygen stable isotopes in minerals. On the basis of the data obtained, an original scheme of the mineral formation history is suggested and physical and chemical conditions of ore deposition and possible sources of fluids are constrained.

GEOLOGICAL SETTING

Regional Geology

The present-day structure of the accretionary-fold belt of Northeastern Russia, which encloses the Mesozoic sequence of the Chukotsk fold region (Fig. 1a), was formed as a result of collision and accretion of heterogeneous blocks of various sizes, which amalgamated to the Eurasian margin during the countermovement of plates of the Pacific and Arctic for a relatively short time from the end of the Jurassic to the beginning of the Cretaceous (Zonenshain *et al.*, 1990). Thick Triassic terrigenous sequences occur in the basement of Mesozoic rocks. The deformation of Mesozoic sedimentary rocks into isoclinic syncline folds and horst-anticlines of northwestern strike and the injection of granitoid intrusions occurred during the Aptian Age (115 Ma ago) at the collision of the Eastern Asian margin with the Chukotka plate, the Kula plate, blocks of the Alazeisk–Oloisk zone, and the Nutesinsk arc. Triassic terrigenous deposits underwent deformation in the Early Cretaceous. Paligenic granite batholiths of the Chukotsk belt are compatible with those of the Kolyma belt and intruded simultaneously or later than deformation events. The collision of the Chukotsk massif with the Siberian plate and the Omolon–Okhotsk massif resulted in the formation of the Yuzhno-Anyuisk suture. During the Albian Age (100 Ma ago), the Chukotsk blocks moved along the Yuzhno-Anyuisk suture relative to Siberia under conditions of confining compression. The collision of Chukotka territory and the Siberian plate and blocks inside the Kolyma plate continued at this time. The formation of the Okhotsk–Chukotsk volcanic belt began in the Albian Age as well. Simultaneously, a subduction zone was created at the margin of Eurasia. The formation of this active margin indicated the termination of the continent collision in the northeast of Russia. The development of the Okhotsk–Chukotsk belt caused the intense tectonomagmatic activization of the southeastern margin of Chukotka, which began in the Early Cretaceous. This led to the intensification of the volcanoplutonic activity and metamorphic and mineral-forming processes.

At present, the territory of Chukotka displays the block structure that resulted from the repeated alternation of tectonic stress fields during the accretion and the tectonomagmatic activization. Blocks were separated by deep transform faults a few hundred kilometers long. Northwestern faults are relatively older. They coincide with the general strike of Mesozoic fold structures and are traced for tens and hundreds of kilometers. Younger faults strike northeast in accord with the structures of the Okhotsk–Chukotsk volcanic belt. Submeridional and sublatitudinal faults that host ores and hydrothermal mineralization (Novozhilov and Gavrilov, 1999) are widespread as well.

Several intrusive complexes and their comagmatic volcanic sequences occur in this region (Volkov and Sidorov, 2001; Goryachev, 1998), namely: (1) Early Cretaceous, (2) Early to Late Cretaceous, and (3) Late Cretaceous magmatic complexes. The first one includes hypabyssal intrusions, subvolcanic bodies, and dikes of monzonites and rhyolites, as well as lavas of intermediate and basic composition displaying high alkalinity and referred to the trachyite–latite series. The second complex, of the late Albian to early Cenomanian ages, includes intrusions and dikes of mainly siliceous and

more rarely intermediate compositions, as well as a thick sequence of ignimbrites of a rhyolite–dacite–andesite association. The Late Cretaceous complex includes extended dike swarms of northeastern and sublatitudinal strikes and small mantos of their comagmatic volcanic rocks of the andesite–basalt and trachybasalt association.

The north, Chukotsk flank of the Okhotsk–Chukotsk volcanic belt is framed with fan-shaped linear zones of tectonomagmatic activization forming a perivolcanic area of this belt. In Central Chukotka, northeastern zones of the tectonomagmatic activization prevail over those transverse to the direction of major fold structures. The extension of these zones is hundreds of kilometers and their width is tens of kilometers. They inherited ancient through fault arrays in the basement and are traced as zones of tensional folding, chains of intrusive–cupola structures, relicts of volcanic depressions, mantos, eruptive and explosive bodies, and dike swarms and are observed as geophysical and geochemical anomalies (Volkov and Sidorov, 2001).

Cupola structures were found within tectonomagmatic activization zones (Gel'man, 1977). Their cores are composed of amphibolite facies rocks such as crystalline schists, gneisses, and amphibolites, while their apical zones and limbs consist of rocks metamorphosed under conditions of the epidote–amphibolite and greenschist facies. Regional metamorphism is considered to have occurred in the Early Cretaceous, while contact metamorphism is believed to be Middle Cretaceous (95.5 Ma ago according to K–Ar data) (Goryachev, 1998). Sidorov and Volkov (2001) assumed that processes of intrusive magmatism, cupola formation, and hydrothermal activity occurred in this region synchronously with the formation of the volcanoplutonic association of the Okhotsk–Chukotsk volcanoplutonic belt. Intrusive–cupola structures control the ore distribution within the tectonomagmatic activization zones. The Kukeneisk satellite structure is an example. In the axial zone of this structure, the Kukeneisk granitoid massif, elongated in the northeastern direction, is outcropped (Fig. 1b). It is located within the Kukeneisk transverse tectonomagmatic activization zone, situated on the western flank of the Palyavaamsk fold zone at the western flank of the Pegtymel'sk volcanic trough of the Okhotsk–Chukotsk volcanoplutonic belt. This structure is confined to the submeridional Keveem–Kukeneisk fault zone (Volkov and Sidorov, 2001). The Maiskoe ore field is located at the intersection of longitudinal northwestern-trending and latitudinal northeastern-trending faults. The Maiskoe gold–sulfide deposit, where disseminated ores are of commercial interest; the large Kukeneisk cassiterite–sulfide deposit; and the epithermal occurrences of Sopka Rudnaya and Promezhutochnoe (Fig. 1b) are known in this ore field.

Geology of the Deposit

The Maiskoe deposit is hosted by a sandstone–siltstone–slate sequence of the Middle Triassic (Fig. 2) that is deformed into small submeridional isoclinic folds. Brachysyncline and brachyanticline structures are revealed on the eastern and northern flanks of the area.

Fracture systems play an important role in the distribution of orebodies. The major submeridional ore-controlling faults are within a tectonic zone of 2–3 km in width. Repeated tectonic activization of this territory led to the renovation of ancient faults and the formation of new faults that mainly extend in the northeastern direction. Displacements of rock blocks occurred along these faults. As a result, several blocks that contain fragments of the fold structures and monoclinal and subhorizontal layered rocks are revealed at the deposit. The most uplifted horst-shaped wedge, of about 5 km^2 in size, where major orebodies are located (Novozhilov and Gavrilov, 1999), is established at the central zone of the deposit. Carbonaceous rocks lie at the base of this wedge.

In the ore-hosting sequence the content of carbonaceous matter in these rocks is tens of wt % on average, but this figure increases up to 1–2 wt % in some places. Sites where the concentration of carbonaceous matter is higher than 50 wt % are rare. The C_{org} ranges from 0.63 to 1.13 wt % and from 0.13 to 0.29 wt % in black siltstones and sandstones, respectively. This value amounts to 2.58 to 2.72 wt % at sites where quartz veinlets are widespread (Shilo *et al.*, 1992). Carbonaceous matter occurs generally as microscopic particles of 0.01–0.1 mm in size disseminated in rocks or as impregnated inclusions distributed along bedding of country rocks. Rare relicts of flora with well-preserved structure of xylene tissue are clearly observed. Carbonaceous matter usually intergrows with pyrite and rarely with arsenopyrite. Diagenetic pyrite that fills in holes in cells or replaces cells of vitrinized vegetative tissues was found in the carbonaceous matter. On the base of optical properties, carbonaceous matter has been identified as vitrinite. Varieties intermediate between amorphous vitrinite and graphite are referred to shungite. Carbonaceous matter is, probably, syngenetic with siltstones.

The country terrigenous rocks are injected by dikes of basic and siliceous rocks that occupy up to 25% of the deposit area. Relationships between magmatic rocks and their K–Ar datings allow one to outline the following sequence of their injection: granodiorite-porphyry and aplite dikes (118–107 Ma) ⟶ granites of the Kukeneisk massif (111–107 Ma) ⟶ lamprophyre dikes (111–106 Ma) ⟶ rhyolite-porphyry subvolcanic bodies (115–97 Ma) ⟶ andesite–dacite and basalt dikes (K_2–P) (Sidorov and Volkov, 2001).

Orebodies

Orebodies are confined to the latitudinal zone of intense tectonic activity 3.5 km long and about 2 km

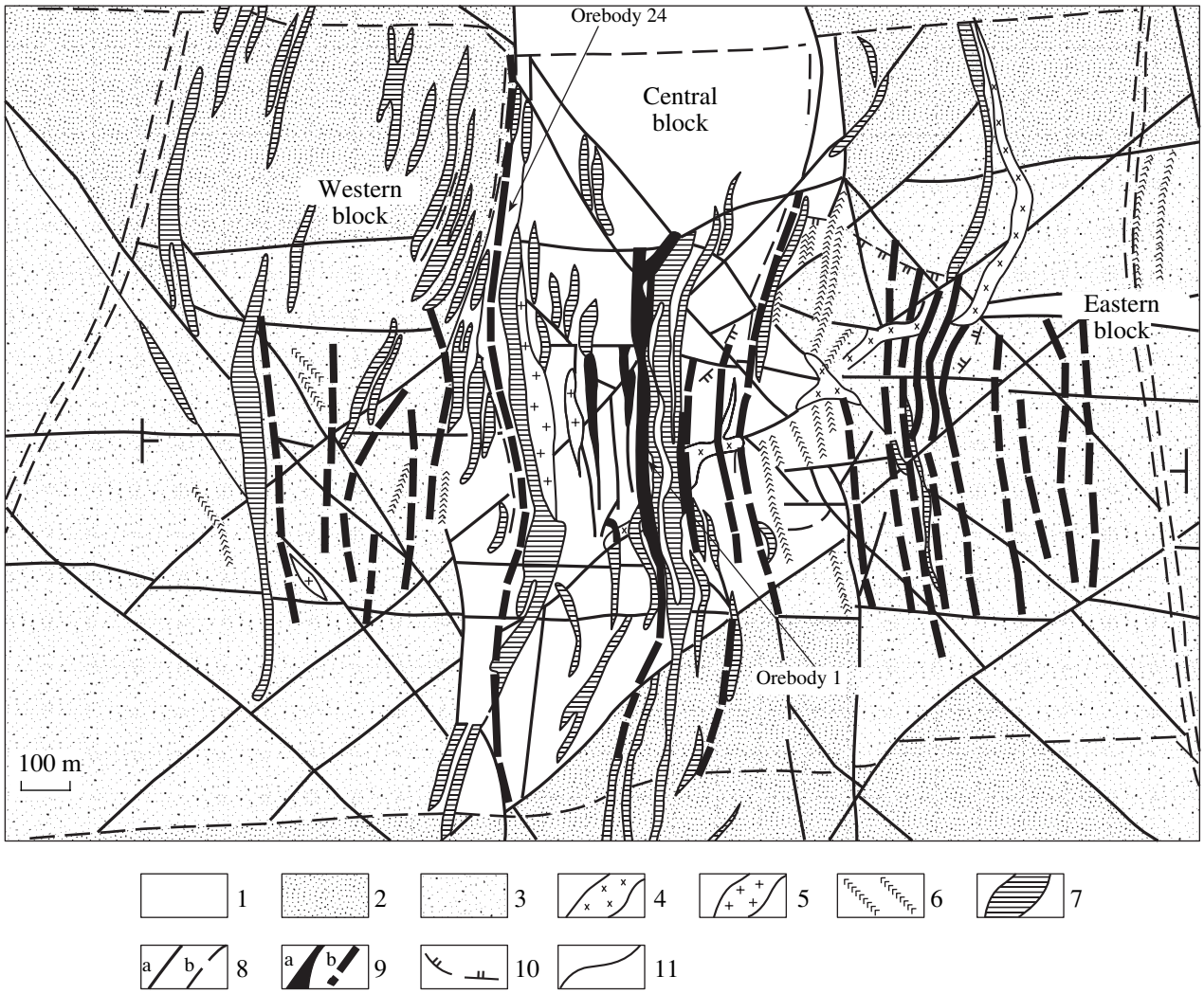

Fig. 2. Schematic geological–structural map of the Maiskoe deposit (after Volkov and Sidorov, 2001). 1—Siltstones, Middle Triassic Keveemsk suite; 2—Middle Triassic sandstones; 3—Triassic interbedding sandstones and siltstones; 4—granodiorites and granite-porphyries; 5—aplites; 6—lamprophyres; 7—rhyolite-porphyries, 8—established (a) and inferred (b) faults; 9—explored (a) and assumed (b) orebodies; 10—contour of sericite metasomatic rocks; 11—geological boundaries.

wide that is restricted with faults on the north and south. Rocks underwent ductile deformations inside this zone. About 30 orebodies of submeridional strike dipping to the east at angles of 85°–75° and 60°–50° were found within this zone.

Orebodies occur in intensely dislocated rocks with fine cleavage fabric that underwent boudinage and contain numerous corrugated veinlets of metamorphogenic quartz.

The morphology of orebodies is variable. Quartz and carbonate–quartz veins and mineralized zones are present.

Mineralized zones contain disseminated gold-bearing pyrite–arsenopyrite mineralization, the intensity of which is gradually decreased from their center to the periphery. A superposition of quartz and quartz–stibnite veins containing visible native gold onto mineralized zones is observed in some places. The largest mineralized zone, labeled as Orebody 1, is traced for 1.5 km along the strike and to a depth of 1 km by drillholes. Its average thickness is 4.3 m. Mineralized zones are located in ductile siltstones on the western flank of the deposit, while veins are predominantly spread in sandstones on its eastern flank. The mineral compositions of veins are more variable than that of mineralized zones.

MINERAL COMPOSITION, MEGASTAGES, AND FORMATION SEQUENCE OF ORES

More than 60 hypogenic minerals have been established at the Maiskoe deposit (Table 1).

Based on original and previously described data on age relationships among mineral aggregates (Fig. 3a),

Table 1. Mineral compositions of orebodies at the Maiskoe deposit

Degree of abundance	Minerals	
	ore minerals	gangue minerals
Major	Pyrite, Arsenopyrite, Stibnite	Quartz, Sericite, Dickite, Kaolinite, Hydromuscowite
Subordinate	Native gold, Sphalerite, Galena, Stannite, Cassiterite, Pyrrhotite, Chalcopyrite, Pb sulfoantimonites (Boulangerite, Zinckenite, Plagionite), Bournonite, Cosalite, Fahlores, Marcasite	Carbonate (Dolomite, Ankerite, Siderite)
Rare	Native bismuth, Native arsenic, Galenobismuthite, Acantite, Andorite, Chalcostibite, Bi sulfotellurides, Tungstenite	Chlorite, Tourmaline

their spatial distribution, and the relation between hydrothermal mineral formation and the development of geological, tectonic, and magmatic processes, we concluded that the Maiskoe deposit formed during three megastages.

Mineralized gold-bearing pyrite–arsenopyrite zones were formed during the auriferous sulfide megastage under conditions of tectonic compression and regional metamorphism of the greenschist facies. K–Ar dating suggests that the latter occurred in the Early Cretaceous (Goryachev, 1998). This megastage originated along submeridional tectonically active zones as a result of metasomatic replacement of country rocks. Mostly it occurs in ductile siltstones, and more rarely, in sandstones on the eastern flank of the deposit.

Different mineral aggregates of the quartz veins, from the early quartz–molybdenite aggregates (Fig. 3b) and the cassiterite–sulfide aggregates to the sphalerite–stannite and galena–bournonite–boulangerite aggregates, were deposited during the next, rare metal megastage. These mineral aggregates are superposed onto the metasomatic mineralized zones. This conclusion is evidenced by thin bands (several millimeters) of fine-grained disseminated pyrite and arsenopyrite aggregates in selvages of quartz veins (Fig. 4) and fragments of brecciaed metasomatic rocks in vein quartz that underwent partial or complete dissolution. The latter caused bird's-eye segregations of relict pyrite and arsenopyrite from the early disseminated ores. The change of the disseminated ores by the quartz veins suggests a change from tectonic compression and ductile deformation to brittle deformation under extension conditions.

The quartz–stibnite veins, which occur predominantly on the western flank of the deposit, were crystallized during the final, gold–stibnite megastage. Cataclasis of disseminated sulfide ores and the cassiterite–sulfide mineral aggregates preceded their formation (Fig. 3a). Therefore, the quartz–stibnite mineralization is superposed onto both metasomatic ore-bearing rocks of the auriferous sulfide megastage and on the quartz–sulfide veins of the rare metal megastage. At the near-contact zone of quartz–stibnite veins, cataclasis of quartz–cassiterite–sulfide veins is often observed. Fragments of these veins, as well as fragments of the country rocks, are cemented by fine-grained laminated aggregates of redeposited pyrite and arsenopyrite (Fig. 3e).

A similar sequence of ore formation was established at the Kukeneisk cassiterite–sulfide deposit, located within the exocontact zone of the Kukeneisk intrusion (Volkov and Sidorov, 2001). Both deposits (Maiskoe and Kukeneisk) occur in the same sandstone–slate sequence, displaying a block structure. Different quantitative relations of the auriferous sulfide and cassiterite–sulfide styles of mineralization are found at these deposits: the auriferous sulfide ores prevail at the Maiskoe deposit, while the cassiterite–sulfide ores are major at the Kukeneisk deposit.

MINERAL ASSEMBLAGES AND CHEMISTRY OF MINERALS

Auriferous Sulfide Megastage

The mineralized zones, which contain the major reserves of gold, were formed during this megastage. The mineralized zones are metasomatically altered rocks consisting of quartz, sericite, fine-grained pyrite and arsenopyrite, and clay minerals. These rocks were predominantly formed after siltstones with a high content of carbonaceous matter. Sulfides form veinlets and disseminated grains. Quartz, iron-bearing dolomite, ankerite, and clay minerals were identified among the gangue minerals of this megastage (Volkov and Sidorov, 2001). These minerals enclose carbonaceous matter as well.

Carbonaceous matter was observed in the mineralized zones as relatively large particles (up to 1 mm) of polygonal or spherical shape. They are often cataclased. They are confined to quartz and quartz–pyrite microveinlets in siltstones. Carbonaceous matter associated with sulfides in quartz microveinlets was formed as a result of redeposition and coarsening of organic matter of country rocks due to their interaction with a hydrothermal fluid.

The quartz–pyrite–arsenopyrite mineral assemblage with finely dispersed gold occurs in nearly all mineralized zones at the deposit. It is most widespread

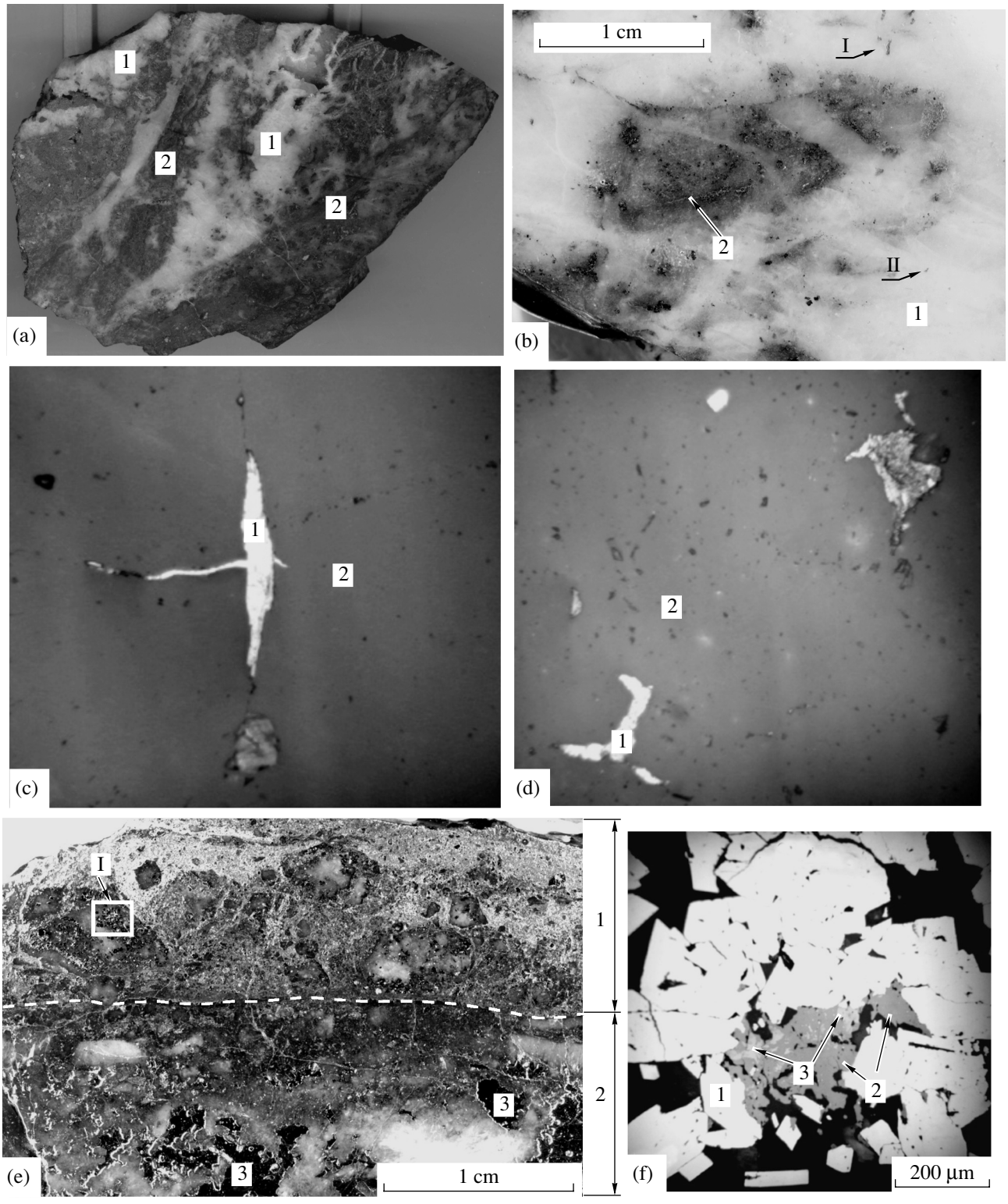

Fig. 3. Relationships of mineral aggregates and minerals in ores of the Maiskoe deposit. a—Quartz–stibnite aggregates (1) cementing fragments of disseminated auriferous sulfide ores (2); b—quartz–molybdenite veins (1) with fragments of sandstones bearing disseminated pyrite and fine needle arsenopyrite I (2); c, d—fragments I and II of Fig. 3b: molybdenite inclusions (1) in quartz II (2); e—contact of brecciaed quartz vein of rare metal megastage (1) with quartz–stibnite vein (2) and fragments of auriferous sulfide ores (3), f—fragment I in Fig. 3d: pyrite–arsenopyrite aggregates (1) are cemented by sphalerite (2)–stannite (3) mineral aggregates.

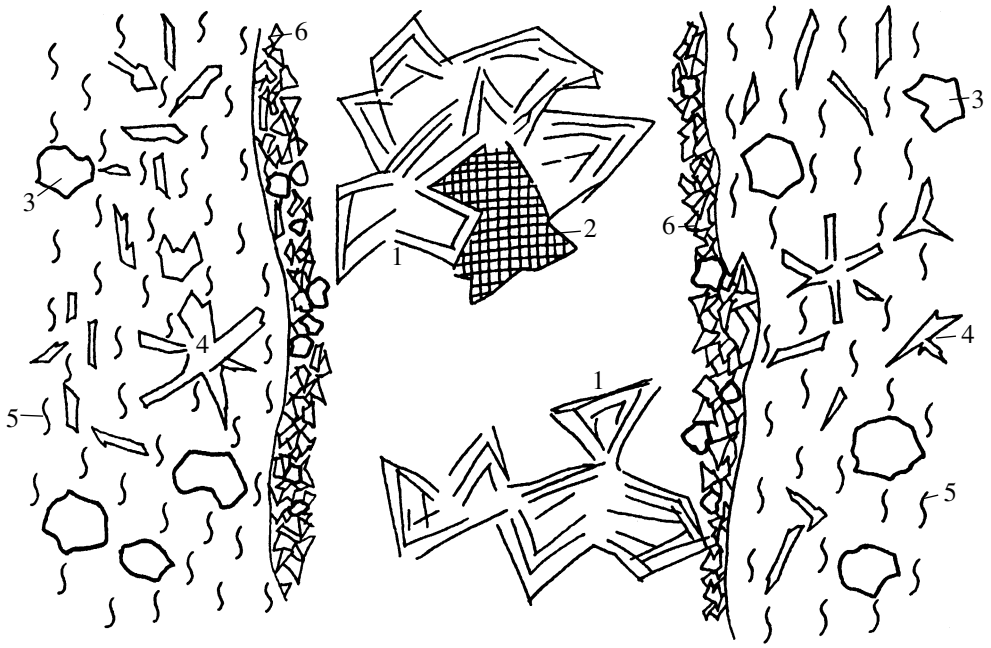

Fig. 4. Schematic sketch of quartz vein of the rare metal megastage of mineralization. Without scale. 1—Nestlike segregation of coarse-grained pyrite II and arsenopyrite II; 2—sphalerite–stannite mineral aggregate; 3—disseminated fine-grained euhedral pyrite; 4—needle arsenopyrite; 5—quartz–sericite metasomatic rocks; 6—abundant disseminated fine-grained aggregates of redeposited pyrite and arsenopyrite.

in Orebody 1. This assemblage was not observed in quartz veins.

Arsenopyrite I occurs as well-shaped needle and elongated prismatic crystals, their aggregates, and veinlets. Fine needle arsenopyrite is widespread at the contact of siltstone fragments and cementing quartz. Arsenopyrite I overgrows pyrite and corrodes it. Sizes of arsenopyrite I range from thousandths up to tenths of a millimeter and rarely amount to 1 mm.

Electron microanalysis showed that the contents of Fe, As, and S in arsenopyrite I range from 33.5 to 36.3 wt %, from 38.7 to 46.00 wt %, and from 20.3 to 24.5 wt %, respectively. The S/As ratio in this mineral varies from 1.054 to 1.482 (Fig. 5). Atomic absorption analysis revealed Ni and Co admixtures in arsenopyrite I. The Ni/Co ratio in this mineral ranges from 0.009 to 3.300. The electron microanalysis showed that gold content in arsenopyrite I varies from the minimum detection limit to 1.2 wt %. The atomic absorption analysis showed that gold content in this mineral ranges from 182.4 to 1030.0 ppm.

Pyrite I forms grains of spherical, cubic, and cubooctahedral shapes. Crystals with well-developed cubic, octahedral, and pentagondodecahedral edges were also found.

An admixture of As up to 6.5 wt % was detected in pyrite I (Table 2). Electron microanalysis showed that the Au content in pyrite I is up to 0.4 wt %, while atomic absorption analysis found 1.44–42.77 ppm. The Ni/Co ratio ranges from 0.145 to 1.505 in pyrite I.

The presence of gold in arsenopyrite I and pyrite I was revealed by analytical techniques only; therefore, it is difficult to suggest an unambiguous conclusion on its mode of occurrence. Arsenopyrite was found to be the major carrier of gold. Native gold was not observed in arsenopyrite grains with the maximal gold content (1.2 wt %) under a microscope with maximal magnifying power. Gold was not recovered from sulfides from the Maiskoe deposit by carnation (Novozhilov and Gavrilov, 1999). A study with a scanning microscope revealed fine-needle arsenopyrite I and pyrite I particles on the surface of crystals. These particles display irregular, sometimes spherical shapes with a maximal size of 6 μm. They are characterized by a high emission of secondary electrons, which is intrinsic to native metals with high atomic numbers. Therefore, it was suggested that they are particles of native gold (Shilo *et al.*, 1992). Gavrilov *et al.* (1982) found segregations of finely dispersed inclusions of native gold in arsenopyrite. It can be suggested that gold occurs in pyrite and arsenopyrite as finest particles (nanoparticles) of native gold. Arsenopyrite may have contained chemically bound gold like that in the Nezhdaninskoe deposit (Genkin *et al.*, 1998). "Invisible" or chemically bound gold is known to be usually incorporated into pyrite with high arsenic amounts (Fleet and Mumin, 1997; Fleet *et al.*, 1993).

Rare Metal Megastage

Textural–structural relationships among mineral aggregates formed during the rare metal megastage

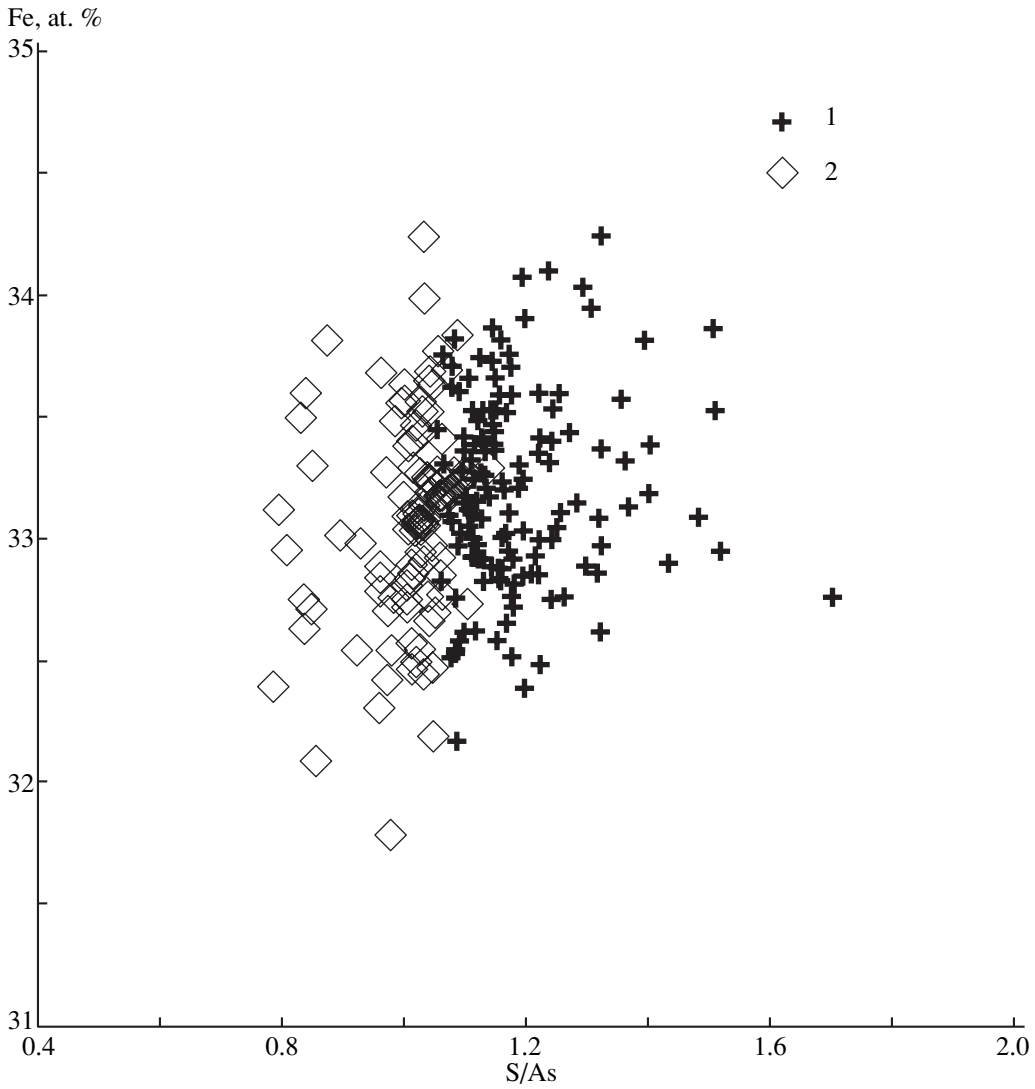

Fig. 5. Plot of Fe and S/As ratios in arsenopyrite of the Maiskoe deposit. 1—Arsenopyrite I; 2—arsenopyrite II.

allowed us to recognize several mineral assemblages replacing each other. Some of them are sporadically met in some orebodies or even their fragments (the quartz–molybdenite and quartz–wolframite assemblages, etc.); others are spread over the whole ore field (for example, the quartz–cassiterite–pyrite–arsenopyrite and stannite–sphalerite assemblages).

The quartz–molybdenite and quartz–wolframite mineral assemblages occur predominantly in the central part of the deposit.

Molybdenite forms rare fine disseminated inclusions in quartz stockwork in sericitolites and granite-porphyries. Quartz–molybdenite veinlets were found in sedimentary rocks and granodiorite-porphyries at a depth of about 1.5 km as well (Volkov and Sidorov, 2001).

Wolframite was found as rare disseminated grains in quartz veins cross-cutting siltstones with auriferous disseminated mineralization.

The cassiterite–pyrite–arsenopyrite assemblage occurs in nearly all quartz veins on the eastern flank of the deposit.

Cassiterite is encountered as isolated crystals or aggregates of its crystals. The size of these crystals is less than 1 mm. Practically always, this mineral is replaced by stannite along cracks and grain margins.

Pyrite II occurs as cubic crystals and granular aggregates, often cataclased. Etching of large pyrite crystals revealed their zonality and rare microblock texture. Sometimes, the core of these crystals is composed of a cubic crystal, which is replaced by a pentagondodecahedral grain in the margin. Spherical inclusions are rarely revealed in cores of cubic and pentagondodecahedral crystals. Electron microanalysis gave up to 0.3 wt % Au in pyrite II. Arsenic was detected in several analyzed grains. Atomic absorption analyses show that the Ni/Co ratio ranges from 0.066 to 10.572 in pyrite II.

Table 2. Chemical compositions of pyrite, wt %

Mineral	Au	Fe	Co	Ni	As	Sb	S	Total
Pyrite I		43.6		0.1	6.1		48.7	98.5
		44.3			6.5		49.4	100.2
		44.9		1.3	1.7	0.1	52.7	100.7
	0.4	45.7			5.1		47.2	98.4
	0.3	46.3					54.7	10.1
	0.5	46.4		0.1	2.8	0.1	49.0	98.9
		48.0		0.2	1.0	0.1	49.8	99.1
	0.1	45.1	0.1	0.1	1.7		52.6	99.7
	0.2	45.2			4.5		49.3	99.2
	0.4	47.1			0.2	0.1	52.8	100.6
		46.7					53.4	100.1
	0.1	47.2			1.4		50.7	99.4
	0.3	46.4	0.1		0.4		53.7	100.9
Pyrite II	0.2	45.2			2.1		51.1	98.6
	0.2	45.5			0.4		52.2	98.3
	0.2	45.7					53.7	99.6
	0.3	45.8					52.4	98.5
		45.9					53.3	99.2
		46.3					52.2	98.5
		46.4					53.2	99.6
	0.4	46.5					52.3	99.2
		47.6					53.1	100.7

Note: Here and in Tables 2–8, analyses were carried out using a Camebax SX-50 electron microprobe. Analytical conditions were as follows: accelerating voltage, 20 kV; current beam, 30 nA; standards: FeS_2 for Fe and S, $AgAsS_2$ for As and Ag, $CuSbS_2$ for Sb and Cu, $AuAgTe_4$ for Au, CoAsS for Co, and NiS for Ni.

Arsenopyrite II forms aggregates of columnar crystals with clearly displayed pseudorhombic shape in quartz veins. The size along their elongation is up to 5–7 mm. Oscillatory zoning, revealed by etching, and polysynthetic and mimetic twins are typical for arsenopyrite II crystals.

The contents of Fe, As, and S in arsenopyrite II vary from 32.8 to 34.9 wt %, from 43.1 to 51.4 wt %, and from 17.0 to 21.4 wt %, respectively (Fig. 5). The S/As ratio in this mineral varies from 1.054 to 1.482. Contents of As and S within the individual crystal vary as well. The S/As ratio decreases from the core of some grains to their margin from 1.152 to 1.098. Arsenopyrite II contains up to 1.5 wt % Sb. Sb contents mostly decrease from 0.3 to 0.2 wt % toward the crystal margins. Ni and Co contents are low in arsenopyrite II relative to arsenopyrite I. Atomic absorption analysis showed that in arsenopyrite II Au content varies from 4.5 to 117.2 ppm, which is one order lower than values for arsenopyrite I.

Löllingite was found in mineral aggregates of the second megastage. Its chemical composition is recalculated to the formula $Fe_{0.99}As_{1.89}S_{0.12}$.

Pyrrhotite is a rare mineral in ores of the deposit. It was found in a thin (up to 2 cm) quartz–sulfide veinlet that contains pyrite, pyrrhotite, chalcopyrite, and Bi and Te minerals. Pyrrhotite underwent an intense desulfidization and is replaced by marcasite–pyrite aggregates with the formation of the typical bird's eye texture. In addition, isolated segregations of pyrrhotite or its intergrowths with chalcopyrite less than 0.1 mm in size were found in large-crystalline aggregates of pyrite and arsenopyrite. Electron microanalyses of this mineral correspond well to a formula of $Fe_{0.89}S$.

Chalcopyrite is associated with pyrrhotite and more rarely with fahlore. It usually forms small grains impregnated in pyrite II, arsenopyrite II and quartz and in carbonate microveinlets cross-cutting pyrite II. Sphalerite stars and rare inclusions of native gold up to 5–8 μm in size were observed in chalcopyrite.

The sphalerite–stannite mineral assemblage occurs in the majority of orebodies.

Structural intergrowths of these minerals indicate that sphalerite and stannite deposited later than chalcopyrite but earlier than galena and Pb and Sb sulfosalts. Relationships between sphalerite and stannite,

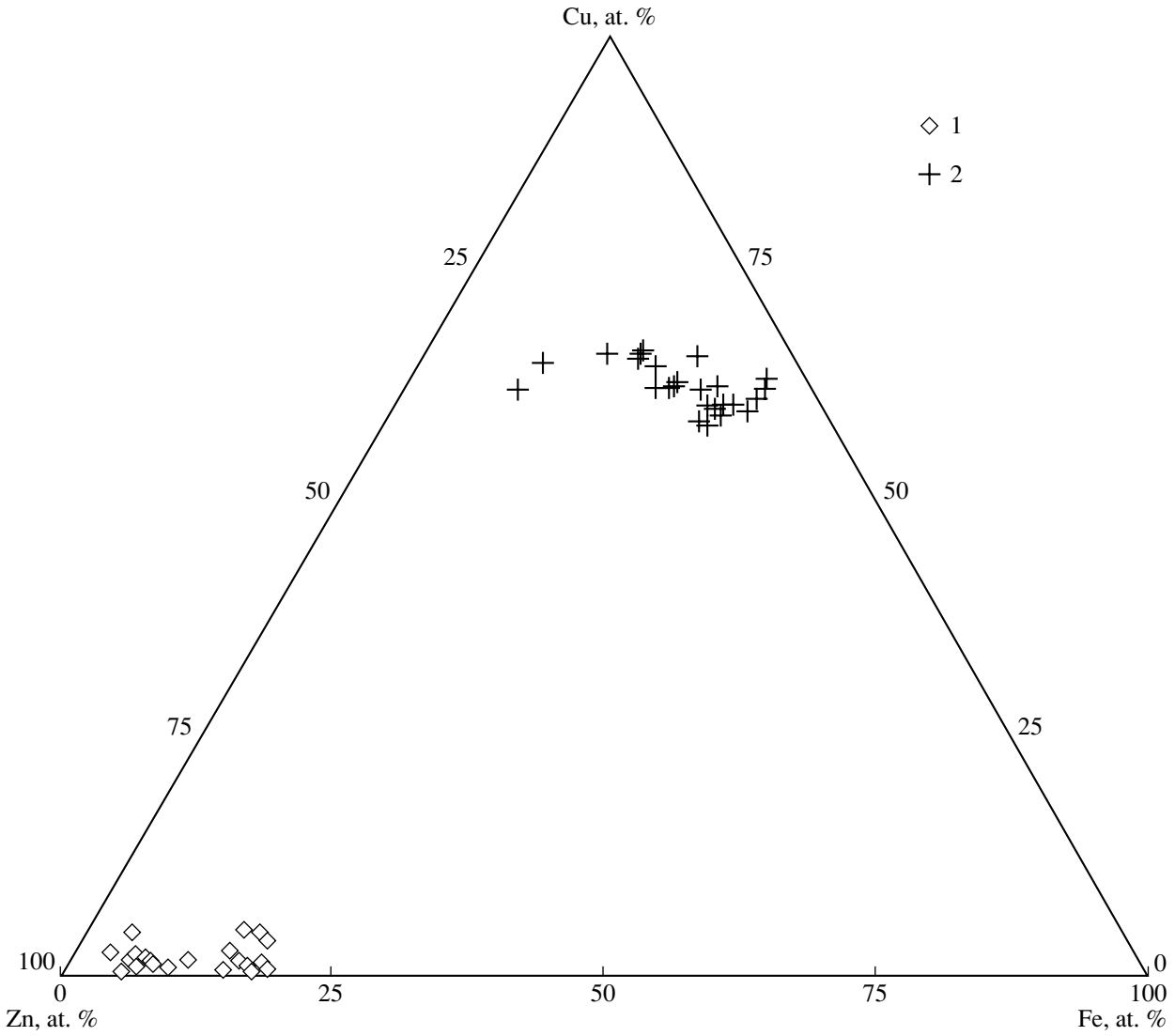

Fig. 6. Compositional plot for stannite and sphalerite of the Maiskoe deposit. 1—Sphalerite; 2—stannite.

grains of which exhibit mutual boundaries, testify to their simultaneous precipitation. However, sphalerite continued to crystallize after the stannite deposition in some cases because it cements aggregates of stannite grains, corroding them. Sphalerite often contains emulsion inclusions of chalcopyrite.

Stannite was commonly observed in intimate intergrowths with *sphalerite*. It forms anhedral grains confined to both interior areas and margins of sphalerite grains. Stannite overgrows cassiterite, replacing it along cracks and grain margins; forms isolated inclusions in quartz and arsenopyrite; overgrows pyrite II and arsenopyrite II; and penetrates the latter along cracks.

The chemical composition of stannite widely varies (Fig. 6). It always contains zinc. Zn content in stannite ranges from 1.6 to 11.8 wt %. Fe content varies from 3.5 to 13.3 wt %.

The chemical composition of sphalerite varies as well (Fig. 6): contents of Zn, Fe, and Cd vary from 51.3 to 62.0, from 1.8 to 10.4, and from 0.6 to 2.8 wt %, respectively. Several analyses gave up to 0.8 wt % Mn, 0.3 wt % Ge, and 0.1 wt % In, respectively. Electron microanalysis revealed up to 2.6 wt % Sn in some grains. Since the isomorphic substitution of Zn for Sn in the crystal structure of sphalerite is extremely limited (Osadchii and Sorokin, 1989), the high Sn content in sphalerite can be explained by the formation of a solid solution with complex tin sulfides the crystal structure of which is similar to that of sphalerite. Minerals of the stannite group are such tin sulfides.

Chemical compositions of coexisting stannite and sphalerite were used to estimate the formation temperatures of the sphalerite–stannite mineral assemblage with the geothermometer suggested by Osadchii and Sorokin (1989). The data obtained showed that their

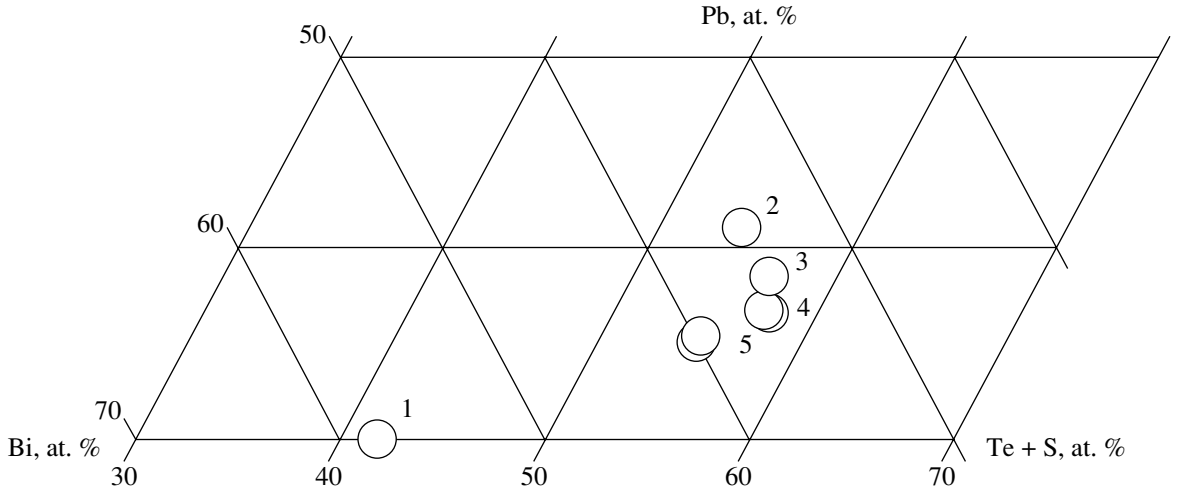

Fig. 7. Compositional plot for bismuth sulfotellurides. 1—Bi_4TeS_2; 2—$PbBi_3(Te, S)_5$; 3—$PbBi_4(Te, S)_7$; 4—$PbBi_6(Te, S)_9$; 5—$PbBi_8(Te, S)_{11}$.

formation temperatures ranged from 194 to 298°C (Table 3) in different orebodies.

The following trends are assumed in the changing of the chemical compositions of minerals of this assemblage during the process of their crystallization, namely: Fe content in sphalerite decreases from 10.4 to 1.8 wt %, while Zn content in stannite decreases from 11.8 to 2.6 wt % and the Fe content increases in this mineral from 3.5 to 13.3 wt % (Fig. 6).

The Bi and Te mineral assemblage was found in quartz veinlets with pyrrhotite. Its position in a scheme of the mineral formation sequence was not established because the relationships of these veinlets with other mineral aggregates were not observed.

Among Bi minerals, native bismuth, bismuthinite, galenobismuthite, and cosalite were found, which often form mutual intergrowths.

Native bismuth was found as microinclusions in bismuth sulfosalts and joseite A. Ag and Hg admixtures were detected in this mineral.

Bismuthinite was observed in intergrowths with bismuth sulfosalts and as individual inclusions in quartz. It contains 0.9 wt % Cu, 3.0 wt % Pb, 0.6 wt % Sb, and 0.4 wt % Se as admixtures. Hg and Ag admixtures were detected in several analyses (Table 4).

Cosalite is the most widespread bismuth mineral in ores of the deposit. It often contains inclusions of galenobismuthite and bismuth sulfotellurides. High contents of Ag (up to 5.3 wt %), Cu (up to 0.7 wt %), and Sb (up to 6.0 wt %) should be pointed out in this mineral. It always contains an admixture of Te (up to 0.4 wt %, 1.4 wt % in several analyses) and Se (up to 0.3 wt %) (Table 4). Silver is considered as a common trace element in cosalite; its concentration amounts often to 3.0 wt % (Karup-Moller, 1977; Mozgova, 1985).

The chemical composition of *galenobismuthite*, which is a rare mineral in this assemblage, is close to its ideal composition (Table 4). Sb and Se admixtures (a few tenths of percent) are detected in this mineral; Hg (up to 0.4 wt %) is sporadically present in galenobismuthite.

It should be noted that an Se admixture was always found in bismuth sulfosalts, although this element was practically not detected in other sulfides.

Lead–bismuth sulfotellurides were observed in association with lead–bismuth sulfosalts. They usually form small inclusions in cosalite. The content of major components in them varies substantially (Table 5, Fig. 7). Pb, Bi, Te, and S contents range from 7.2 to 16.6, from 53.4 to 61.0, from 22.2 to 30.0, and from 5.8 to 7.3 wt %, respectively. Common trace elements whose concentrations are tenths of percent were detected in these minerals, including Sb, Se, Ag, Cu, and more rare Hg. X-ray powder diffraction was not carried out due to small grain sizes and their intimate mutual intergrowths. An analysis of the mineral that does not contain lead was satisfactorily recalculated to the joseite A formula of Bi_4TeS_2. A mineral with a composition close to kochkarite ($PbBi_4Te_7$) was also revealed. This mineral contains S, which distinguishes it from kochkarite. The other analyses were recalculated to the following ideal formulas: $PbBi_6(Te, S)_9$, $PbBi_7(Te, S)_{11}$, and $PbBi_8(Te, S)_{11}$ with variable Te/S ratios. Compositional variations could be partly related to the phase nonhomogeneity found in some samples by scanning microscopy. Natural minerals of such a composition are unknown.

Native gold II associates with bismuth minerals. It forms rare spherically shaped inclusions less than 8.0 μm in size in chalcopyrite. Fineness of this mineral is 773‰ (Table 6).

The galena–bournonite–boulangerite association occurs in ores everywhere but is manifested insignificantly. An exception is Orebody 14, where this associ-

Table 3. Chemical compositions of coexisting sphalerite and stannite from the Maiskoe deposit (wt %), distribution constants (K_D), and their formation temperatures

Mineral	Sample nos.	Cu	Zn	Cd	Fe	Mn	Sn	Ge	S	Total	K_D	*T*, °C
Sphalerite	Msk-80	0.8	54.3	1.5	10.2		0.6	0.2	33.4	101.0	0.037	217
Stannite	″	28.1	2.6	0.2	13.3		26.6	0.1	30.9	101.8		
Sphalerite	″	0.3	53.6	1.4	10.2		0.9		34.1	100.4	0.035	212
Stannite	″	27.9	2.6	0.1	14.1		26.7	0.2	30.5	102.1		
Sphalerite	″	2.5	51.8	1.2	9.6		1.4		32.7	99.2	0.033	207
Stannite	″	28.4	2.2	0.2	12.6		26.5	0.1	30.5	100.5		
Sphalerite	″	0.7	56.5	1.3	8.7		0.3	0.1	33.8	101.4	0.037	216
Stannite	″	27.5	3.2	0.3	13.2		26.8	0.2	30.9	102.1		
Sphalerite	″	3.1	52.3	1.2	8.0		2.0		32.8	99.4	0.028	194
Stannite	″	28.0	2.4	0.2	12.9		26.7	0.2	29.2	99.6		
Sphalerite	Msk-89	1.1	56.8	0.8	6.1	0.5	0.1		33.8	99.2	0.046	235
Stannite	″	28.2	4.7	0.3	10.8	0.1	27.2	0.1	30.2	101.6		
Sphalerite	″	1.2	57.8	0.9	5.7	0.8	0.2		33.8	100.4	0.042	226
Stannite	″	28.7	4.6	0.1	10.8	0.2	26.9	0.2	30.0	101.5		
Sphalerite	″	0.6	60.9	1.1	3.7	0.7	0.1	0.1	33.2	100.4	0.044	230
Stannite	″	27.8	6.4	0.4	9.0	0.2	27.4		29.8	101.0		
Sphalerite	″	0.9	60.0	0.7	3.1	0.5	0.3	0.1	33.9	99.5	0.043	229
Stannite	″	29.2	6.4	0.4	7.7	0.2	27.7		29.8	101.4		
Sphalerite	″	0.6	60.8	0.9	3.2	0.5	0.1	0.2	33.4	99.7	0.039	220
Stannite	″	28.8	6.0	0.5	8.1	0.2	27.4	0.3	29.8	101.1		
Sphalerite	″	1.1	58.1	0.8	3.8	0.5	0.4	0.2	33.1	98.0	0.046	234
Stannite	″	28.4	5.9	0.4	8.4	0.2	27.7	0.2	29.5	100.7		
Sphalerite	Msk-95	1.4	59.6	1.9	3.5	0.7	0.3	0.2	33.1	100.7	0.070	273
Stannite	″	29.0	7.6	0.8	6.4	0.2	27.9	0.1	29.9	101.9		
Sphalerite	″	0.9	58.0	2.1	4.2	0.6	0.1	0.2	33.1	99.2	0.071	276
Stannite	″	28.3	7.0	0.8	7.1	0.2	27.3		30.0	100.7		
Sphalerite	″	1.5	60.1	1.2	3.2	0.4	1.0	0.2	33.6	101.2	0.086	295
Stannite	″	28.5	9.1	0.6	5.7	0.1	27.4	0.1	29.9	101.4		
Sphalerite	″	0.6	60.2	1.3	3.9	0.4	0.1		33.8	100.3	0.051	244
Stannite	″	29.2	6.1	0.5	7.7	0.2	27.7	0.1	30.3	101.8		
Sphalerite	″	0.7	54.8	1.6	9.0	0.2	0.1	0.2	33.3	99.9	0.072	277
Stannite	″	27.2	5.3	0.2	12.1		25.3	0.2	30.9	101.2		
Sphalerite	2M-31	1.6	54.8	2.1	8.1	0.2	0.1		33.1	100.0	0.051	243
Stannite	″	28.3	3.9	0.2	11.4		26.8	0.1	29.0	99.7		
Sphalerite	″	0.7	54.2	2.4	9.6	0.2	0.2		33.5	100.8	0.053	247
Stannite	″	27.5	3.7	0.2	12.4		26.6		29.9	100.3		
Sphalerite	″	0.6	52.5	2.6	9.9	0.2		0.1	33.3	99.2	0.068	271
Stannite	″	27.3	4.4	0.1	12.2		26.8	0.1	30.1	101.0		
Sphalerite	″	0.3	52.7	2.8	9.8	0.2		0.1	33.9	99.8	0.088	298
Stannite	″	26.7	5.4	0.4	11.4		26.8	0.1	29.7	100.5		
Sphalerite	″	0.4	52.5	2.6	10.3	0.2	0.1	0.2	33.2	99.5	0.068	271
Stannite	″	28.1	4.3	0.1	12.3		26.5	0.3	29.8	101.4		
Sphalerite	″	0.5	51.7	2.6	10.4	0.2	0.3		32.8	98.5	0.070	274
Stannite	″	27.8	4.2	0.2	12.0	0.1	26.7		29.4	100.4		
Sphalerite	M-354	0.4	55.3	2.0	8.2	0.2			32.4	98.5	0.058	255
Stannite	″	27.5	4.7	0.2	11.9	0.1	26.3		29.8	100.5		
Sphalerite	″	0.8	53.4	2.1	9.4	0.2			33.3	99.2	0.076	283
Stannite	″	26.4	5.2	0.3	12.1		25.3	0.3	29.7	99.3		
Sphalerite	″	0.7	55.3	2.1	7.1	0.2	0.1		33.2	98.7	0.044	230
Stannite	″	27.8	4.1	0.3	11.9	0.1	26.8		29.9	100.9		

Note: Analytical conditions were as follows: accelerating voltage, 20 kV; current beam, 30 nA; standards: SnS for Sn, ZnS for Zn and S, $CdIn_2S_4$ for In and Cd, FeS for Fe, CuS for Cu, GeS for Ge and Mn. The compositions of sphalerite and stannite were determined at the contact zones of these minerals; the distance between two points of analyses was less than 5 μm. $K_D = (Fe/S)_{in\ sphalerite}/(Fe/Zn)_{in\ stannite}$ of reaction: $Cu_2FeSnS_4 + ZnS = Cu_2ZnSnS_4 + FeS$. Temperatures were calculated after the sphalerite–stannite geothermometer of [T°C = 1274/(1.174) – logK_D] (Osadchii and Sorokin, 1989).

Table 4. Chemical compositions of sulfides and sulfosalts of bismuth of the Maiskoe deposit, wt %

Mineral	Ag	Cu	Pb	Sb	Bi	Se	Te	S	Total
Bismuthite	0.1			0.1	81.8	0.4	0.1	18.3	100.8
		0.9	3.0	0.1	78.1	0.3		18.7	101.1
Galenobismuthite	0.1		27.1	0.2	55.5	0.2	0.1	17.1	100.3
		0.1	27.9	0.5	54.3	0.2	0.1	16.5	99.8
			27.5	0.5	54.5	0.2		16.5	99.7
Cosalite	3.5	0.5	33.0	6.0	39.5	0.2	0.2	17.5	100.4
	2.0	0.5	37.0	4.9	39.1	0.1	0.2	17.0	100.8
	3.6	0.1	39.0	2.6	38.9	0.3	0.4	16.3	101.2
	4.9	0.1	34.0	2.8	42.5	0.2	0.3	16.8	101.6
	3.1		36.6	0.1	42.6	0.3	1.4	15.6	99.7
	3.5		37.6	0.1	42.8	0.2	0.3	15.8	100.3
	1.4	0.4	36.9	0.7	43.3	0.2	0.1	15.9	98.9
	5.3	0.5	31.9	1.2	46.0	0.2	0.2	16.0	101.3

Note: Analytical conditions were as follows: accelerating voltage, 20 kV; current beam, 30 nA; standards: $AgSbS_2$ for Ag, Bi_2Se_3 for Bi and Se, Sb_2S_3 for Sb, PbSe for Pb, HgTe for Hg, FeS for Fe, and CuS for Cu.

Table 5. Chemical compositions of bismuth sulfotellurides of the Maiskoe deposit, wt %

Mineral	Ag	Cu	Hg	Pb	Sb	Bi	Se	Te	S	Total
Zhozeit A						83.6	0.8	9.3	6.6	100.3
$PbBi_3(Te, S)_5$		0.1		16.6		53.4	0.4	22.2	7.0	99.7
$PbBi_4(Te, S)_7$	0.2	0.1	0.5	12.5	0.4	54.7	0.3	25.5	7.3	101.5
$PbBi_6(Te, S)_9$	0.1		0.3	9.8	0.2	54.2		30.0	5.9	100.5
	0.1	0.1		9.7	0.3	55.2	0.3	28.0	6.5	100.2
$PbBi_8(Te, S)_{11}$				7.4	0.1	59.9	0.3	26.4	5.8	99.9
				7.6	0.1	58.3	0.4	25.9	5.7	98.0
	0.1			7.2	0.1	61.0	0.3	25.7	5.8	100.2

Note: Analytical conditions were as follows: accelerating voltage, 20 kV; current beam, 30 nA; standards: Bi_2Se_3 for Bi and Se, $CuSbS_2$ for Cu, Sb, and S; HgTe for Hg and Te; $AgSbS_2$ for Ag; and PbS for Pb.

ation is relatively wide. Major minerals are galena, sphalerite II, lead sulfoantimonites, and fahlore I.

Galena is a common mineral in ores of the deposit. It forms individual grains in quartz and pyrite, intergrowths with sphalerite, and overgrows arsenopyrite. Galena grains are replaced by lead sulfoantimonites along their margins. Microveinlets composed of galena and sphalerite cut pyrite.

Ag, Sb, and Bi admixtures were detected in galena. The content of isomorphic admixtures is insignificant in galena.

Fahlore I occurs in association with chalcopyrite in pyrite II and in arsenopyrite II. Fahlore I is tetrahedrite containing 27.2–30.2 wt % Sb and up to 9.2 wt % Ag (Table 7). As content is equal to 1.7 wt %. Results of electron microanalysis were recalculated to the formula $((Cu_{8.66–9.95}Ag_{1.50–0.05})_{\Sigma 10.00–10.20}(Fe_{0.64–2.00}Zn_{1.41–0.01}Hg_{0–0.04})_{\Sigma 2.05}(Sb_{3.76–4.19}As_{0.39–0.01}Bi_{0.01–0.04})_{\Sigma 4.19–4.21}(S_{12.13–13.04}Se_{0–0.01})_{\Sigma 12.14–13.04})$.

Boulangerite, zinckenite, and plagionite, as well as *bournonite*, were identified among lead sulfoantimonites, associated predominantly with galena. The mentioned minerals replace galena grains along margins and cracks. Their disseminated needle inclusions are rarely observed in carbonate and fill in intergranular spaces in quartz. Zinckenite was found in intergrowths with cosalite and galenobismuthite, as well at the contact between quartz and stibnite.

Results of electron microanalysis (Tables 7, 8) correspond to ideal formulas of these minerals. An Ag admixture in these minerals should be noted.

Andorite, which is replaced by lead sulfoantimonites and was deposited later relative to these minerals, was found in the discussed assemblage. Results of electron microanalysis (Table 8) satisfactorily fit an empirical

Table 6. Chemical compositions of native gold, wt %

Mineral, mineral assemblage	Au	Ag	Cu	Hg	Total	Fineness, ‰
Native gold II, sulfotellurides and sulfobismuthites of Pb	75.6	20.8	1.2	0.2	97.8	773
Sulfoantimonites of Pb	84.5	16.7		1.4	102.6	824
	87.9	12.2	0.1	0.4	100.6	874
	89.4	11.0	0.1	0.7	101.2	883
Native gold III, chalcostibite, fahlores	92.6	7.9	0.1	0.4	101.0	917
	91.7	8.4	0.1	0.2	100.4	913
	88.8	9.1		0.1	98.0	906
	91.6	9.1	0.1	0.9	101.7	901
	89.3	9.4		0.6	99.3	899
	90.2	9.9		0.6	100.7	896
	88.3	9.6		0.8	98.7	895
Native gold III, stibnite, native arsenic	94.4	7.6		0.3	102.3	923
	92.8	7.8	0.1	0.4	101.1	918
	91.3	8.0		0.6	99.9	914
	92.2	8.1	0.6	0.1	101.0	913
	91.9	8.1		0.8	100.8	912
	91.8	7.9		1.5	101.2	907
	89.7	7.9		1.5	99.1	905
	87.9	9.7		0.2	97.8	899
	87.7	12.4		0.3	100.4	874

Note: Analytical conditions were as follows: accelerating voltage, 20 kV; current beam, 30 nA; standards: Au–Ag alloys containing 90 wt % Au, HgTe for Hg, and pure metallic copper for Cu.

formula of $Ag_{0.91}Cu_{0.02}Hg_{0.01}Pb_{1.02}Sb_{2.97}As_{0.03}Bi_{0.01}Te_{0.01}S_{6.00}$, which corresponds to the ideal formula of $AgPbSb_3S_6$ suggested for this mineral. X-ray powder diffraction proved that this mineral has the andorite-type crystal structure.

A Pb–Sb–Bi–S mineral phase was found at the contact between two different-age assemblages—the lead sulfoantimonite one (zinckenite) and bismuth sulfosalts (cosalite). Results of electron microanalysis were satisfactorily calculated to the formula of $Pb_{5.12}(Sb_{4.16}Bi_{3.81})_{\Sigma 7.98}S_{16.70}$, which allows us to consider this phase as a Bi variety of plagionite ($Pb_5Sb(Bi)_8S_{17}$).

Gold–Stibnite Megastage

The quartz–stibnite assemblage with native gold is one of the latest in the mineral depositional sequence at the deposit. It is spatially closely associated with disseminated ores of the auriferous sulfide megastage, is located in fractures, and forms open-space filling veins; veinlet arrays; and zones of brecciation, where siltstone fragments with early auriferous mineralization are cemented by quartz–stibnite aggregates.

Stibnite and native gold, which associate with fahlore, chalcostibnite, and rarely with chalcopyrite, are the major minerals in this assemblage.

Stibnite is one of most widespread minerals at the deposit. This mineral composes massive granular aggregates, nests, and impregnated grains in quartz. It was rarely observed as druselike segregations or radiative aggregates of elongated prismatic or needle crystals. The size of these crystals varies from fractions of a millimeter to 3–5 cm along the elongation. Stibnite displays evidence for different deformations such as bending, slipping, chipping, and fracturing, as well as growth and polysynthetic twinning.

Finely grained "ricelike" quartz formed after stibnite. Native arsenic overgrows on stibnite. Native gold III associates with stibnite and is commonly confined to the contacts of this mineral with quartz.

Electron microanalysis showed that stibnite contains 71.6 wt % Sb, 27.3 wt % S, and 0.4 wt % As (average of five analyses). These contents are close to the ideal composition of this mineral. Hg (0.4 wt %) and Bi (0.7 wt %) were detected in several analyses. The mineral contains trace elements Ag, Cu, Zn, Fe, and Se as well.

Fahlore II is observed as small inclusions in quartz, intergrowths with native gold III, and inclusions in this mineral. The chemical composition of fahlore II is sig-

Table 7. Chemical compositions of fahlores and copper sulfoantimonites from the Maiskoe deposit, wt %

Mineral	Ag	Cu	Hg	Pb	Zn	Fe	As	Sb	Bi	S	Total
Fahlore I	2.8	34.8	0.4	0.2	3.9	3.4	0.4	29.5	0.2	24.8	100.4
	2.2	36.0		0.2	4.7	3.5	0.6	29.2	0.2	22.4	99.0
	0.6	36.6	0.3	0.1	0.5	6.2	0.1	30.2	0.1	24.5	99.2
	0.7	37.9	0.2			6.6		30.1	0.5	24.5	100.5
	0.4	37.6		0.1	5.5	2.1	0.1	29.5	0.4	24.7	100.4
	0.5	37.6			0.5	6.2	0.1	28.9	0.4	24.9	99.1
	0.5	37.4			0.1	6.7	0.1	29.3	0.1	24.6	98.8
	3.4	34.4	0.4	0.1	2.1	5.6	0.2	29.3	0.1	24.7	100.3
	8.0	32.3		0.1	4.9	2.2	1.7	26.7	0.1	24.0	100.0
	9.2	31.3			4.7	2.5	1.5	27.3	0.3	22.7	99.5
Fahlore II	2.0	38.2		0.1	5.0	2.5	8.8	17.1		25.2	98.9
	2.1	39.0	0.1	0.2	4.7	2.9	10.2	15.5	0.1	25.8	100.6
	2.2	38.5	0.4		4.7	3.0	10.7	15.1	0.1	25.6	100.3
	0.4	39.8		0.1	5.0	2.8	10.3	15.5	0.1	26.1	100.1
	0.4	40.3	0.2		5.4	2.3	9.2	17.4	0.2	25.6	101.0
	0.4	38.8			4.9	2.5	7.5	19.3	0.1	25.4	98.9
	2.2	37.2			4.8	2.7	7.4	18.8		25.8	98.9
Bournonite	0.1	12.7		41.9			0.1	26.0	0.1	20.4	101.3
		12.6	0.1	41.6				24.8	0.3	19.6	99.0
		12.6	0.2	41.6			0.1	26.1	0.4	18.9	99.9
Chalcostibite	0.1	25.7	0.3	0.1		0.3	0.2	49.5	0.4	25.1	102.0
		24.9				0.3	0.3	49.2	0.4	24.8	99.9
		24.9	0.3	0.1			0.2	49.7	0.1	25.2	100.5

Note: Analytical conditions were as follows: accelerating voltage, 20 kV; current beam, 30 nA; standards: $AgAsS_2$ for Ag and As, Bi_2Se_3 for Bi and Se, Sb_2S_3 for Sb, PbSe for Pb, HgTe for Hg and Te, FeS for Fe, CuS for Cu, and ZnSe for Zn.

nificantly different from that of fahlore I: contents of Sb and As range from 15.1 to 19.3 wt % and from 7.4 to 10.7 wt %, respectively (Table 7). This mineral displays higher Zn content and lower Fe content. Results of electron microanalysis of fahlore II were calculated to the formula of $(Cu_{9.50–10.07}Ag_{0.05–0.34})_{\Sigma 9.84–10.12}(Fe_{0.65–0.84}Zn_{1.31–1.15}Hg_{0-0.03})_{\Sigma 1.96–2.02}(Sb_{1.98–2.57}As_{2.28–1.60}Bi_{0-0.01})_{\Sigma 4.18–4.26}(S_{12.67–13.07}Se_{0.03–0})_{\Sigma 12.70–13.07}$.

Among minerals of the tetrahedrite–tennantite series, zincian tetrahedrite is commonly considered to have crystallized earlier than iron tetrahedrite, sometimes enriched in silver (Spiridonov, 1987; Moralev *et al.*, 1988). In ores at the Maiskoe deposit, the opposite depositional sequence of these minerals was established: crystallization of iron tetrahedrite (fahlore I) was replaced by zincian tetrahedrite and tennantite. Fahlore II is observed in association with visible native gold in those areas of quartz–stibnite veins in which fragments of siltstones containing abundant disseminated fine needle arsenopyrite with finely dispersed native gold are preserved as bird's eye breccias.

Chalcostibite forms anhedral grains intergrown with native gold III, fahlore II, and stibnite.

This mineral crystallized probably at an interaction between fahlore and stibnite.

Native gold III forms intergrowths with stibnite chalcostibite and fahlore and rarely with chalcopyrite. This mineral was observed in intimate association with segregations of native arsenic in quartz–stibnite veins.

Fineness of native gold III ranges from 824 to 923‰ (Table 6). This mineral always contains an Hg admixture, ranging from 0.1 to 1.5 wt %. The maximal content of this element was detected in grains associated with native arsenic or in areas where this mineral occurs. A Cu content of 1.2 wt % was detected in native gold III. Bi, Se, and Te contents amount to a few tenths of percent in some analyses.

Native arsenic occurs in orebodies 1 and 9. It forms disseminated grains in quartz–stibnite veins and overgrows on stibnite, often near grains of native gold III, but intergrowths with the latter were not observed. It is confined to bird's eye breccias in quartz–stibnite veins, where they intergrow sometimes with fine needle arsenopyrite I. It occurs as rounded anhedral grains.

Table 8. Chemical compositions of lead sulfoantimonites and andorite, wt %

Mineral	Ag	Cu	Hg	Pb	As	Sb	Bi	Se	Te	S	Total
Boulangerite				53.4	0.1	26.0	0.6			18.9	99.0
	0.1		0.4	52.7		25.9	0.2		0.1	18.7	98.1
				54.9	0.6	25.1	0.2		0.1	18.9	99.8
		0.1	0.2	54.4	0.3	25.6	0.2	0.1		18.7	99.6
		0.1		55.6	0.4	25.8	0.1	0.1	0.1	19.1	101.3
Plagionite			0.8	41.7	0.2	36.9	0.2	0.1	0.1	21.1	101.1
			0.5	40.3	0.2	37.1	0.1			20.8	99.0
				40.7	0.2	36.5	0.2	0.1		21.0	98.7
			0.2	40.2	0.2	37.6	0.1			20.6	98.9
				40.7	0.2	36.5	0.2	0.1		21.0	98.7
Zinckenite	0.2	0.3		30.2	0.1	37.1	12.0			22.0	102.0
	0.4	0.7		32.0	0.6	44.0	0.1			21.4	99.2
	0.3	0.5	0.4	31.5	0.4	42.8	0.2			22.5	98.6
	0.3	0.6	0.3	32.0	0.6	42.8				22.4	99.0
	0.3	0.6		32.5	0.6	43.8				22.5	100.3
Andorite	11.3	0.2	0.2	23.7	0.3	41.0	0.2		0.1	21.9	98.9
	11.2	0.2		24.0	0.2	40.9	0.1		0.1	21.9	98.6
	11.5	0.1	0.1	24.6	0.2	40.8	0.3			22.2	99.8
	11.3	0.1	0.3	25.4	0.2	41.4	0.2	0.1	0.1	21.7	100.8
	11.2	0.1		24.8	0.2	40.6	0.2	0.1	0.1	21.3	98.6

Note: Analytical conditions were as follows: accelerating voltage, 20 kV; current beam, 30 nA; standards: $AgAsS_2$ for Ag and As, Bi_2Se_3 for Bi and Se, Sb_2S_3 for Sb, PbSe for Pb, HgTe for Hg and Te, FeS for Fe, and CuS for Cu.

Hg (up to 0.5 wt %), Sb (1.1 wt %), S (up to 0.6 wt %) and Se (0.2 wt %) are contained in native arsenic.

Fine flake aggregates of *tungstenite* overgrow on and penetrate intergranular spaces of wolframite. It contains 1.7–1.8 wt % Fe and tenths of percent of Mo, Sb, and Mn.

Thus, differences in chemical compositions of some minerals and modes of occurrences of some elements were found in mineral assemblages that deposited during different megastages. If gold precipitated as nanoparticles (?) or was incorporated into the composition of pyrite or arsenopyrite at the auriferous sulfide megastage, it occurs as a native mineral in later ores. Arsenic-bearing pyrite was found among mineral assemblages of the early megastage. The cassiterite–sulfide mineralization is gold-bearing also because small grains (3–8 μm) of native gold with fineness 773‰ were found in chalcopyrite from the pyrrhotite–chalcopyrite mineral assemblage. Bismuth mineralization is widespread in the center and on the eastern flank of the deposit, while antimony mineralization occurs predominantly on the western flank of the deposit, where it is superposed often onto the auriferous sulfide mineral association of the first megastage. This process was accompanied by the partial recrystallization of sulfides of generation I, which resulted in mobilization of some amount of finely dispersed gold and its redeposition as larger grains of native gold of high fineness in association with stibnite, tetrahedrite, and chalcostibite. Arsenic-bearing tetrahedrite found in this assemblage, possibly, incorporated arsenic liberated during the dissolution of early arsenopyrite.

FLUID INCLUSIONS

A study of fluid inclusions was carried out using double-polished thin sections 0.3–0.5 mm thick. Fluid inclusions were viewed in more than 500 thin sections prepared from quartz samples collected in mineralizations of different megastages. Fluid inclusions suitable for microthermometric measurements were found in 50 double-polished thin sections that represent 17 samples.

Description of Fluid Inclusions

Fluid inclusions 3–25 μm in size in quartz display the shape of negative crystals or irregular shape. On the basis of their trapping time, fluid inclusions were subdivided into primary, pseudosecondary, and secondary inclusions. Primary fluid inclusions are uniformly distributed in the host mineral. Pseudosecondary fluid inclusions are confined to cracks that do not cross-cut boundaries of a quartz grain. Fluid inclusions healing

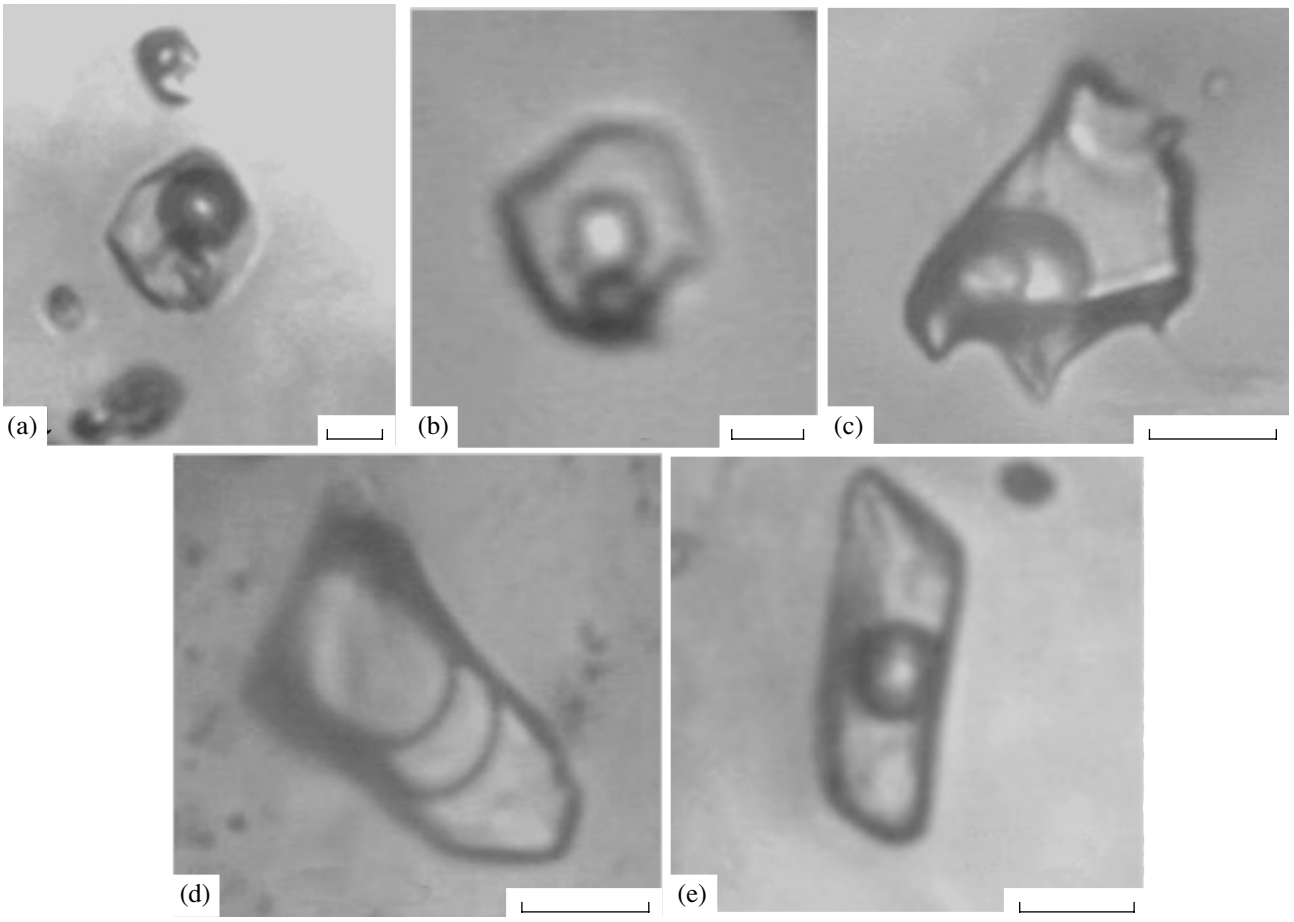

Fig. 8. Types of fluid inclusions in quartz from the Maiskoe deposit. a—Type I (polyphase fluid inclusions); b—type 2 (three-phase fluid inclusions); c—type 3 (three-phase H_2O-rich fluid inclusions); d—type 4 (three-phase vapor-rich fluid inclusions); e—type 5 (two-phase fluid inclusions). Bar length, 10 μm.

cracks in quartz are referred to secondary ones. As a rule, irregular shapes are typical for secondary fluid inclusions.

Fluid inclusions were subdivided into five types (Fig. 8) based on their phase compositions at room temperature.

Type I includes polyphase fluid inclusions (Fig. 8a). They contain solid phases (a cubic isotropic mineral with a large volume, one or two small well-soluble phases), aqueous solution, and a vapor bubble that contains liquid CO_2. Such fluid inclusions were found in quartz from the cassiterite–pyrite–arsenopyrite assemblage (rare metal megastage) in Orebody 10.

Type 2 includes three-phase fluid inclusions that contain a solid phase (a cubic isotropic mineral identified as halite on the basis of proximity of its index of refraction to that of quartz and the formation of hydrohalite on freezing of these fluid inclusions), aqueous solution, and a vapor bubble that does not contain liquid CO_2 (Fig. 8b). Fluid inclusions of this type were found in quartz of the sphalerite–stannite assemblage of the rare metal megastage in Orebody 10.

Type 3 includes three-phase H_2O-rich fluid inclusions that contain aqueous solution and a vapor bubble with liquid CO_2 (Fig. 8c). Such fluid inclusions were found in quartz of the auriferous sulfide, quartz–wolframite, cassiterite–pyrite–arsenopyrite, pyrrhotite–chalcopyrite, sphalerite–stannite, and telluride–bismuthite–cosalite mineral assemblages of the rare metal megastage.

Type 4 includes three-phase vapor-rich fluid inclusions (Fig. 8d). Both vapor and liquid CO_2 and a meniscus of an aqueous solution were observed in these fluid inclusions. As a rule, they were simultaneously trapped with fluid inclusions of type 3, being confined to the same growth zone in quartz.

Type 5 includes two-phase fluid inclusions that contain aqueous solution and a vapor bubble (Fig. 8d). Fluid inclusions of this type are syngenetic to those of type 4. They were found in quartz of the pyrrhotite–chalcopyrite, sphalerite–stannite, telluride–bismuthite–cosalite, galena–bournonite–boulangerite, and gold–quartz–stibnite mineral assemblages.

Microthermometric Studies

The behavior of fluids trapped by fluid inclusions on freezing and heating was studied using a Linkam THMSG-600 stage permitting measurements at temperatures from –196 to +600°C. Compositions of major salt components trapped in these fluid inclusions were estimated on the basis of their eutectic temperatures (Borisenko, 1977). The salt concentration in fluids contained in polyphase and three-phase fluid inclusions was estimated using the dissolution temperature of the halite cubic crystal and calculation for the $NaCl–H_2O$ system (Bodnar and Vityuk, 1994). This value in fluids in two-phase fluid inclusions was estimated using ice melting temperatures known for the $NaCl–H_2O$ system (Bodnar and Vityuk, 1994). Salt contents in fluids with high CO_2 contents were calculated using the melting temperatures for clathrate (Collins, 1979; Darling, 1991). It was impossible to estimate salt contents in dense $CO_2–CH_4$ fluids in some inclusions because the melting temperature of clathrate was higher than +10°C. In this case, salt contents in fluids were estimated using the ice melting temperatures corrected on the basis of measurement of volume ratios of CO_2 and aqueous phases and calculations of the CO_2 concentrations in the fluid. CH_4 contents were estimated from the volume ratios and methane density in the vapor phase, which is related to the partial pressure of methane, which depends on the melting temperature of methane gas hydrates (above +10°C; Claypool and Kaplan, 1974). Corrections taking into account the content of H_2O in gas hydrates were calculated on the basis of these data and the salt content in the $CO_2–CH_4–H_2O$ fluids was estimated. This allowed us to estimate approximately the salt content; however, it was not possible to calculate this value in fluids of such composition. Major components and water were analyzed with a help of a Tsvet 100M model 163 gas chromatograph using a scheme and analytical techniques described previously (Mironova *et al.*, 1992). Anions in fluids were determined with a help of a Tsvet 3006 ion chromatograph (Savel'eva *et al.*, 1988). Minimum detection limits for gaseous components were as follows (*l*): 0.1 for N_2, 4×10^{-2} for CH_4, 3×10^{-2} for CO_2, and 5×10^{-5} for H_2O. Minimum detection limits for anions (F^-, Cl^-, SO_4^{2-}, NO_3^-, NO_2^-, $H_2PO_4^-$, and Br^- (μm/ml)) were 1×10^{-3}. Fluid pressure was estimated at the intersection of isochors obtained from a study of vapor-rich fluid inclusions and isotherms derived from the homogenization temperatures of syngenetic H_2O-rich fluid inclusions (Kalyuzhnyi, 1982).

Results of the microthermometric studies are shown in Table 9 and Fig. 9.

The homogenization temperature of type I fluid inclusions was 535–495°C. CO_2 in these inclusions homogenized in liquid at +30.2°C. An occurrence of halite crystals in these fluid inclusions indicates that NaCl is a predominant salt dissolved in the fluid. Because halite crystals dissolved at +292°C, the salt content in this fluid was estimated as 37.5 wt % NaCl-equiv. The estimated fluid density is 0.88–0.87 g/cm^3.

Type 2 fluid inclusions homogenized at 170°C. The eutectic temperature of –28°C permitted us to assume that dissolved NaCl and $MgCl_2$ were predominant salts in the aqueous solution. The dissolution of the halite crystal at 163°C indicates that the salt concentration in the trapped fluid was 30.2 wt % NaCl-equiv. Its density was estimated as 1.12 g/cm^3.

Homogenization of type 3 fluid inclusions occurred at 430–238°C. The eutectic temperature of –20 to –35°C indicates that dissolved NaCl and $MgCl_2$ prevail in the fluid. The CO_2 melting occurred at –57.3 to –58.8°C. These values are below the melting temperature of pure CO_2 (–56.6°C), which indicates an admixture of gaseous components, particularly, methane, the melting temperature of which is low. The CO_2 and CH_4 concentrations were estimated as 5.2–1.6 mol/kg of solution and 1.6–0.6 mol/kg of solution, respectively. Clathrate is melted at 7.8–11°C. The fluid salinity estimated from clathrate melting temperatures (7.8–9.8°C) was equal to 8.8–2.2 wt % NaCl. The fluid density was equal to 1.00–0.78 g/cm^3.

Gas chromatography showed an admixture of CH_4 and N_2 ranging up to 2.0 mol % and 2.3 mol %, respectively, in the vapor phase trapped by fluid inclusions. Ion chromatography proved the presence of chlorine and admixtures of fluorine and sulfate ion up to 0.18 and 0.24 g/kg of H_2O, respectively.

Melting of CO_2 in type 4 fluid inclusions occurred at –57.3 to –58.8°C. This value is below the melting temperature of pure CO_2 (–56.6°C). CO_2 homogenized in liquid phase at 20.7–25.9°C and in vapor phase at 23.3–30.2°C. The density of CO_2 contained in vapor-rich fluid inclusions is estimated as 0.72–0.22 g/cm^3.

Type 5 fluid inclusions homogenized at 333–119°C. Eutectic temperatures equal to –20 to –31°C indicate that NaCl and $MgCl_2$ are the predominant salts in the aqueous fluid trapped by these fluid inclusions. Ice melting occurred at –0.4 to –6.7°C. These data permitted us to estimate the salt content in the trapped fluid at 0.7–10.1 wt % NaCl-equiv. The density of the aqueous fluid ranges from 0.70 to 0.96 g/cm^3.

It can be assumed that the study of fluid inclusions suggests an involvement of fluids with contrasting chemical and phase compositions. The mineral formation occurred from chloride brines with high salt (37.5–30.2 wt % NaCl-equiv.) and carbon dioxide contents. Two immiscible fluids with different phase composition—a low to moderate saline (2.2–8.8 wt % NaCl-equiv.) $H_2O–CO_2$ fluid with low CH_4 content and a vapor CO_2-rich fluid with low H_2O and CH_4 content—were simultaneously involved in the mineral-forming system. This conclusion is evidenced by the coexisting fluid inclusions of types 3 and 4 simultaneously trapped on quartz crystallization. The aqueous saline fluid, with

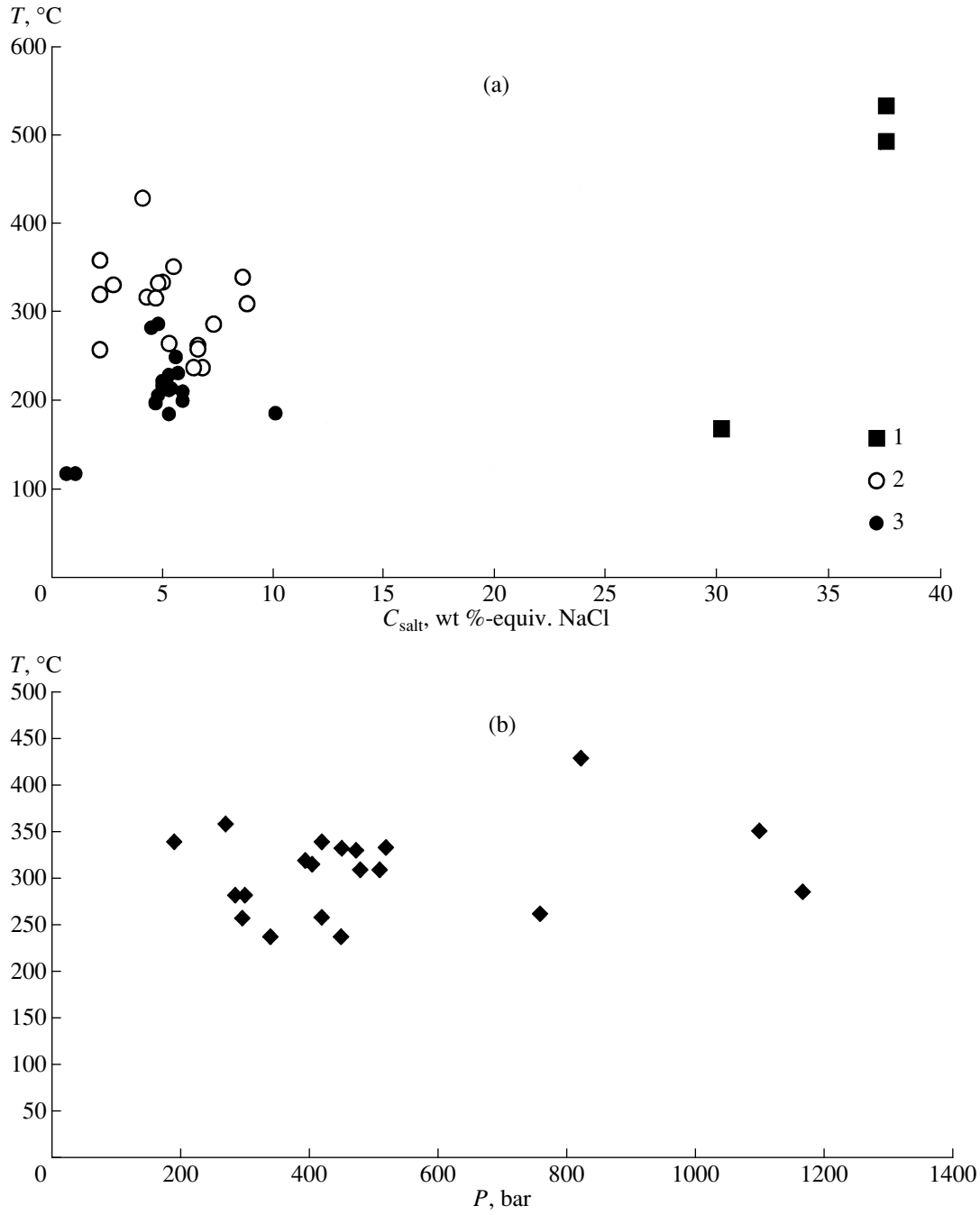

Fig. 9. Temperature–salinity (a) and temperature–pressure (b) plots based on fluid inclusion study in quartz from the Maiskoe deposit. 1–3—Fluid type: 1—brine, 2—H_2O–CO_2 fluid, 3—dilute aqueous fluid.

a salt content ranging from 0.7 to 10.1 wt % NaCl-equiv., penetrated simultaneously with the CO_2-rich vapor fluid with low CH_4 content in this mineral-forming system. This conclusion is supported by the finding of coexisting syngenetic fluid inclusions of types 4 and 5.

The above data differ from the physicochemical parameters and chemistry of the fluids published previously (Goncharov, 1983; Volkov and Sidorov, 2001). It was supposed that the temperature of mineral-forming fluids was below 400°C and fluid salinity was higher than 12 wt % NaCl-equiv. and that minerals were deposited mainly from the fluids with salt contents of 20 wt % NaCl-equiv.

SULFUR AND OXYGEN STABLE ISOTOPES

Oxygen and sulfur isotope ratios were studied in quartz and sulfides, respectively, from auriferous sul-

Table 9. Results of heating and freezing studies of fluid inclusions in quartz from ore veins at the Maiskoe deposit (Chukotka)

Sample no.	Orebody	Type of fluid inclusions*	*n*	T_{Hom}, °C	T_{Eut}, °C	$T_{ice\ melt}$ (NaCl), °C	$T_{melt\ CO_2}$, °C	$T_{Hom}\ CO_2$, °C	$T_{clathrate\ melt}$, °C	C_{salt}, wt % NaCl-equiv.	C_{CO_2}, mol/kg of solution	C_{CH_4}, mol/kg of solution	*d*, g/cm^3	*P*, bar	$\frac{P_{total}}{P_{H_2O}}$
79	1	2**	3	287	–29	–6.2	–57.7	26.2 L	9.4	7.3	5.2	0.8	0.97	1170	17.4
		2**	2	–	–	–	–57.9	24.5 L	–	–	–	–	0.72		
		2**	6	283	–31	–2.7	–	–	–	4.5	–	–	0.79	300…	4.8…4.5
		2**	5	–	–	–	–58.0…–57.9	23.2…24.5 V	–	–	–	–	0.24…0.22	285	
123/2	1	3	4	119	–21	–0.6…–0.4	–	–	–	1.1…0.7	–	–	0.95	–	–
64/1	1–2	2**	4	310	–33	–7.9	–57.8	23.3 V	10.6	8.8	3.6	1.6	0.81	510…	5.6…5.3
		2**	7	308 V	–	–3.5	–58.1…–58.0	26.6…30.2 V	–	5.7	–	–	0.37…0.35	480	
		3	2	187	–31	–6.7	–	–	–	10.1	–	–	0.96	–	–
65	2	2**	11	342 V	–30	–2.5	–58.1	25.2 V	11.0	3.4	4.5	2.1	0.70	430	3.0
		2**	4	281	–35	–5.9	–57.5	29.2 V	9.8	8.1	2.5	0.7	0.93	1100	18.0
		2**	3	–	–	–	–58.0	25.3 L	–	–	–	–	0.71		
80	6	2**	8	263	–30	–5.3	–58.8	26.8 V	9.8	6.6	2.8	0.7	0.94	760…	15.2…
		2**	6	259	–30	–5.3	–58.8	26.7 V	9.8	6.6	2.8	0.7	0.95	420	14.1
		2**	5	–	–	–	–58.8	20.7…25.9 L	–	–	–	–	0.60…0.43		
		2**	6	238	–31	–5.5	–58.6	28.5 V	9.8	6.8…6.4	2.5	0.6	0.95	450…	11.3…8.9
		2**	5	–	–	–	–58.6…–58.5	27.7…28.9 L	–	–	–	–	0.40…0.35	340	
		3	8	230	–31	–3.2	–	–	–	5.3	–	–	0.88	–	–
10	7	3	7	250	–26	–3.4	–	–	8.6	5.6	–	–	0.84	–	–
		3	9	232	–29	–3.5	–	–	8.8	5.7	–	–	0.86	–	–
		3	4	211	–30	–3.6	–	–	–	5.9	–	–	0.90	–	–
		3	7	201	–22	–3.6	–	–	–	5.9	–	–	0.91	–	–
98/2	9	2**	5	430	–30	–3.1	–57.7	29.0 V	7.9	4.1	4.6	1.1	0.82	820	2.3
		2**	8	–	–	–	–58.0	29.2 V	–	–	–	–	0.32		
		3	2	213	–29	–3.2	–	–	–	5.3	–	–	0.90	–	–
72	9	2**	4	359 K	–33	–1.3	–57.9	–5.5 V	9.8	2.2	–	–	0.08	270	1.6
		2**	2	340	–32	–6.1	–58.7	1.9 V	7.8	8.6	1.6	0.9	0.80	420…	3.0…1.9
		2**	7	317	–32	–5.3	–58.7	15.7 V	7.8	4.3	2.0	0.8	0.85	190	
		2**	4	–	–	–	–58.5	25.2 V	–	–	–	–	0.25		
		3	5	215	–30	–3.3	–	–	–	5.4	–	–	0.89	–	–
		3	3	207	–31	–2.9	–	–	–	4.8	–	–	0.90	–	–
93/2	9	2**	4	331	–30	–2.7	–57.9	27.2 V	8.6	2.8	4.6	1.4	0.76	470	3.8
		2**	2	–	–	–	–57.6	28.6 V	–	–	–	–	0.30		
		3	3	287	–28	–2.9	–	–	–	4.8	–	–	0.79	–	–
		3	12	223	–28	–3.0	–	–	–	5.0	–	–	0.88	–	–
		3	2	218	–28	–3.0	–	–	–	5.0	–	–	0.89	–	–

Table 9. (Contd.)

Sample no.	Ore-body	Type of fluid inclusions*	n	T_{Hom}, °C	T_{Eut}, °C	$T_{ice\ melt}$ (NaCl), °C	$T_{melt\ CO_2}$, °C	$T_{Hom}\ CO_2$, °C	$T_{clath\text{-}rate\ melt}$, °C	C_{salt}, wt % NaCl-equiv.	C_{CO_2}, mol/kg of solution	C_{CH_4}, mol/kg of solution	d, g/cm^3	P, bar	$\frac{P_{total}}{P_{H_2O}}$
81	9	2**	2	305	–35	–6.2	–57.5	26.6 V	9.8	8.4	2.6	0.9	0.88	1110…1080	12.6…12.3
		2**	5	–	–	–	–57.6…–57.3	27.2…27.6 L	–	–	–	–	0.67		
		2**	3	295	–35	–5.2	–57.6	29.0 L	7.8	6.7	4.0	0.6	1.00	910	11.9
		2**	8	–	–	–	–58.1…–58.0	29.5 L	–	–	–	–	0.62		
		2	11	265	–30	–3.6	–57.4	22.2 V	9.4	5.3	2.2	0.7	0.89	–	–
		3	7	209	–32	–3.3	–	–	–	5.4	–	–	0.90	–	–
		3	3	207	–32	–3.2	–	–	–	5.3	–	–	0.90	–	–
126	10	1	8	535	–19	(292)	N.d.	30.2 L	–	37.5	–	–	0.87	–	–
		1	3	507	–19	(292)	″	30.2 L	–	37.5	–	–	0.88	–	–
		1	6	495	–19	(292)	″	30.2 L	–	37.5	–	–	0.88	–	–
		2**	3	352	–31	–4.4	–57.8	26.7 V	10.2	5.5	3.6	1.4	0.78	1100…	7.5…
		2**	15	334	–33	–4.2	–57.8	26.8 V	9.8	5.0	3.5	1.2	0.78	520	3.5
		2**	15	–	–	–	–58.6…–57.9	22.9 L…27.2 V	–	–	–	–	0.60… 0.33		
		3	19	186	–28	–3.2	–	–	–	5.3	–	–	0.92	–	–
		1	5	170	–28	(163)	–	–	–	30.2	–	–	1.12	–	–
27	14	2**	16	322	–32	–6.8	–57.1	27.1 V	9.0	8.8	3.2	1.0	0.84	1240…	11.2…
		2**	7	–	–	–	–57.8…–57.6	26.2…29.8 L	–	–	–	–	0.69…0.60	990	8.9
		2**	4	313	–35	–5.3	–58.0	26.2 V	9.4	7.4	2.4	0.7	0.90	920	9.0
		2**	3	–	–	–	–57.9	30.1 L	–	–	–	–	0.59		
		2	6	259	–33	–5.5	–57.9	28.0 V	9.8	7.8	2.0	0.6	0.96	–	–
		3	7	245	–29	–4.2	–	–	–	6.7	–	–	0.87	–	–
2	Adit 2	3**	12	333	–31	–2.9	–	–	4.8	4.8	–	–	0.70	450…	3.5…
		3**	2	320	–31	–2.8	–	–	4.8	4.7	–	–	0.71	405	4.0
		3**	11	316	–20	–2.8	–	–	4.8	4.7	–	–	0.71		
		3**	8	–	–	–	–59.2…–59.1	27.6…27.3 V	–	–	–	–	0.28		
		2**	2	320 V	–20	–1.3	–59.0	26.2 V	–	2.2	–	–	0.26	390	3.6
		2**	3	258 V	N.d.	N.d.	–59.0	27.1 V	–	–	–	–	0.27	300	7.2
		3	7	199	–21	–2.8	–	–	–	4.7	–	–	0.90	–	–
		3	4	198	–20	–2.8	–	–	–	4.7	–	–	0.90	–	–

Note: * 1, chloride brine; 2, aqueous carbon dioxide fluid; 3, dilute aqueous fluid; **, boiling fluid; n, number of fluid inclusions studied; d, fluid density; homogenization of liquid CO_2 into liquid (L) and vapor (V).

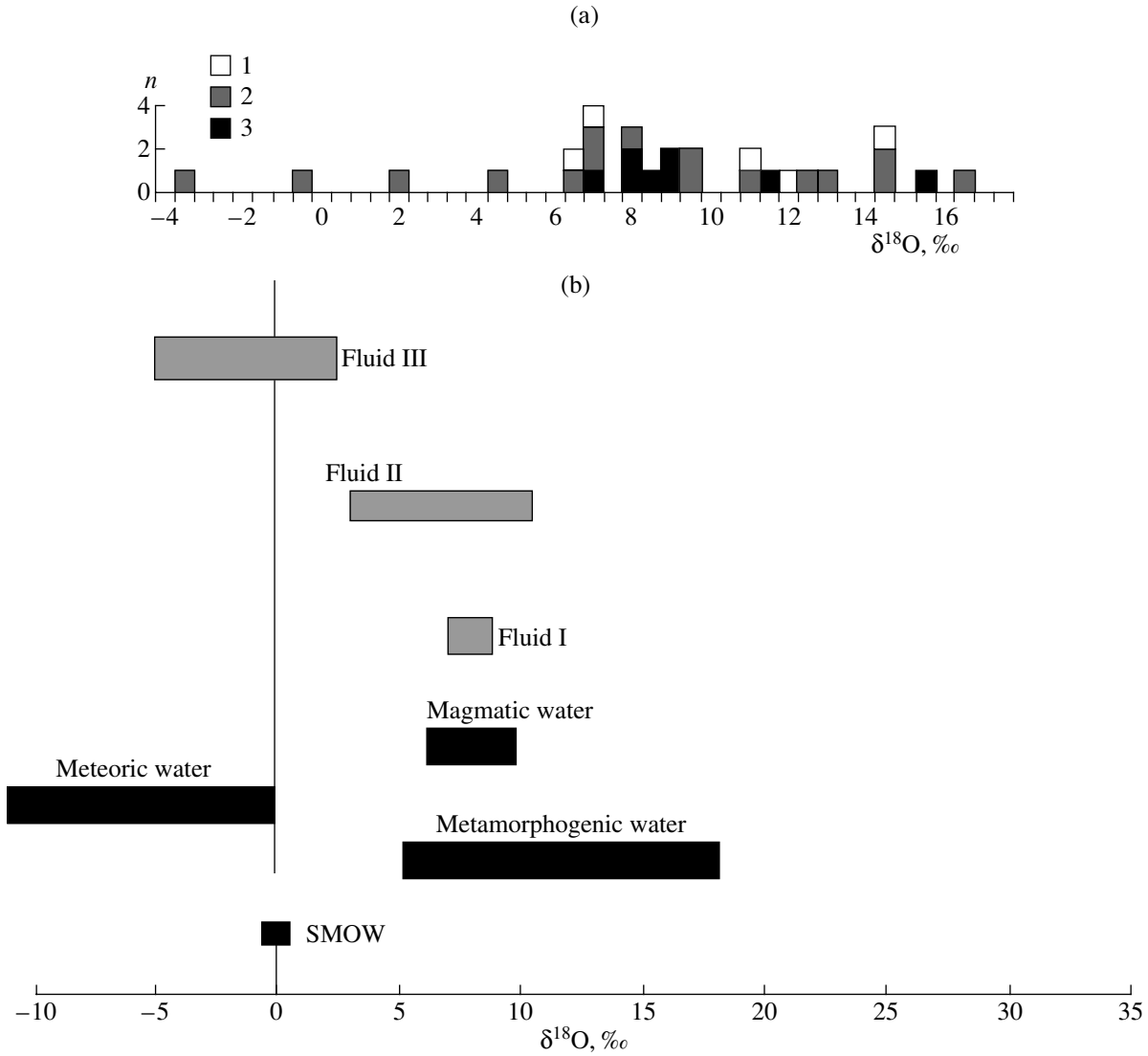

Fig. 10. Oxygen isotope compositions of quartz (a) and mineral-forming fluid (b). 1–3—Ore formation megastages: 1—auriferous sulfide, 2—rare metal, 3—gold–stibnite.

fide, rare metal, and quartz–stibnite aggregates collected from several orebodies (nos. 1, 2, 6, 9, 10, 20, and 23) at the deposit. Mineral fractions were handpicked under a binocular microscope. Monofractions of minerals of one generation were mostly prepared. However, taking into account that mineral aggregates of the different megastages were usually superimposed in orebodies, admixtures of minerals of another generation could be present in samples analyzed. The oxygen isotope compositions were measured for the CO_2 gas released on the interaction of quartz with BrF_5 at 600°C and heated later with graphite rods. The sulfur isotope ratio was measured for SO_2 gas that was obtained on the oxidation of sulfides during interaction with CuO at 1010°C. Isotopic data are reported in standard δ notation relative to the Vienna Standard Mean Oceanic Water (SMOW) for oxygen and the Canyon Diablo troilite (CDT) standard for sulfur. Duplicate measurements of the same samples and standards showed that inaccuracy of the δ value was below ±0.2‰.

Oxygen Isotope Compositions of Quartz and Fluid

The oxygen isotope compositions of quartz deposited at the auriferous sulfide, rare metal, and gold–stibnite megastages are shown in Fig. 10a. The $\delta^{18}O$ values of quartz I, quartz II, and quartz III are +11.8…+14.5‰, +6.4…+16.1‰, and +6.4…+15.2‰, respectively.

Oxygen isotope compositions of water in the mineral-forming fluid equilibrated with quartz of different generations were calculated using the $\delta^{18}O$ of quartz and the mineral formation temperatures estimated from the fluid inclusion study and the equation of the isotope fractionation (Ohmoto and Rye, 1979; Clayton *et al.*, 1972).

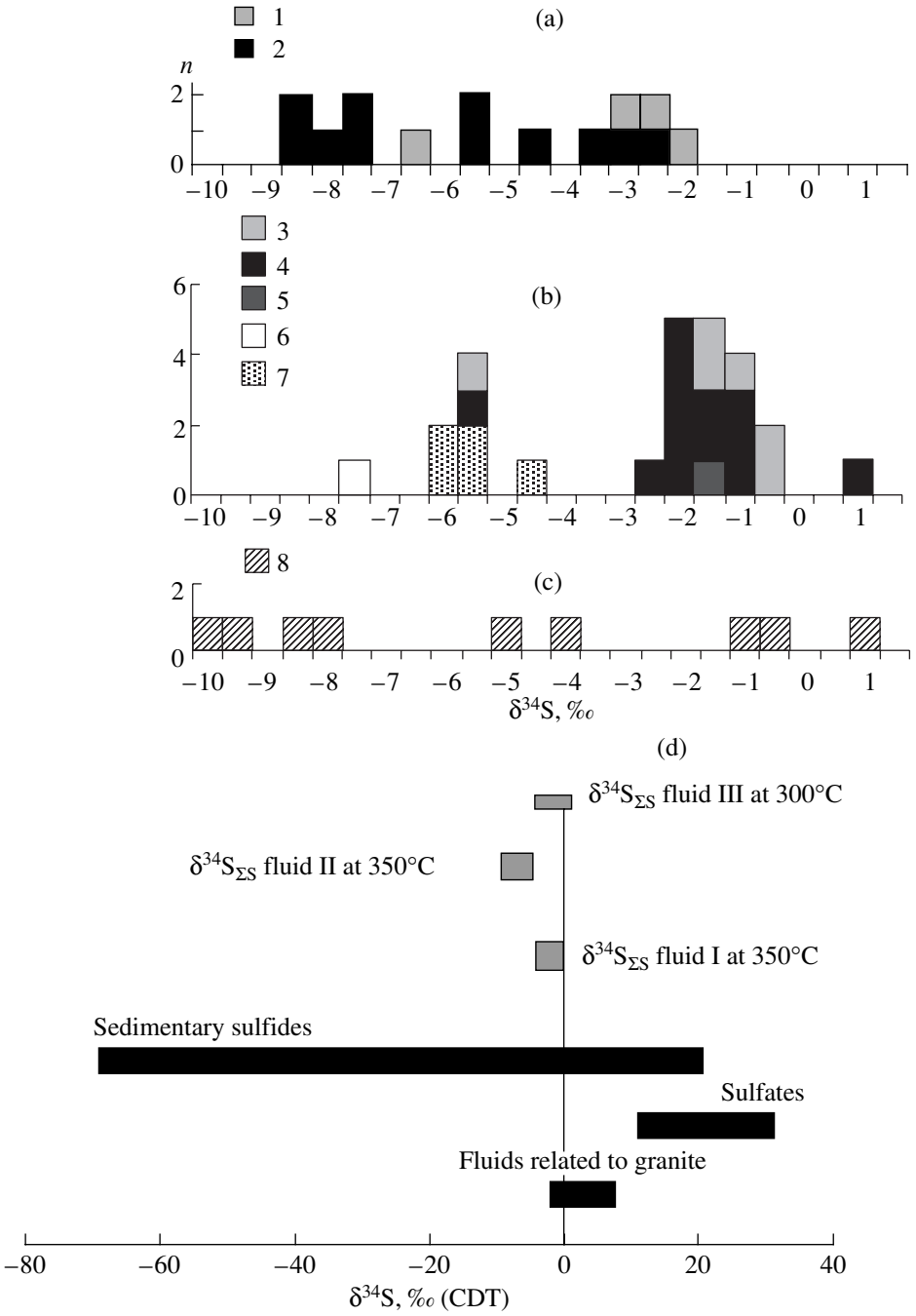

Fig. 11. Sulfur isotope compositions. a—Auriferous sulfide megastage: 1—arsenopyrite I, 2—pyrite II; b—rare metal megastage: 3—arsenopyrite II, 4—pyrite II, 5—sphalerite, 6—galena, 7—sulfosalt; c—gold–stibnite megastage: 8—stibnite; d—mineral-forming fluid.

The $\delta^{18}O$ value of water that deposited quartz I at a temperature of 300°C is equal to +6 ± 2‰ (Fig. 10b). This value falls in the $\delta^{18}O$ value range between +5.5 and +9.5‰, ascribed to magmatic water (Ohmoto, 1986). The $\delta^{18}O$ value of water in the fluid that deposited the cassiterite–sulfide mineralization of the rare metal megastage at 400°C lies between +2.3 and +10.4‰. The $\delta^{18}O$ value of water in the fluid that deposited the quartz–stibnite veins at 200°C ranges from –5.1 to +3.5‰.

Sulfur Isotope Compositions of Sulfides and Fluids

Sulfur isotope compositions were determined for 50 mineral fractions of sulfides (pyrite, arsenopyrite, sphalerite, galena, and stibnite) from the auriferous sulfide, rare metal, and quartz–stibnite ores (Fig. 11a). The

$\delta^{34}S$ values obtained for pyrite I and arsenopyrite I from the auriferous sulfide megastage are close and range from –8.9 to –2.9‰ and –6.9 to –2.4‰, respectively. Sulfur isotope compositions ($\delta^{34}S$) of pyrite II and arsenopyrite II from the cassiterite–sulfide megastage are –5.6 to +0.8‰ and –5.9 to –0.6‰, respectively. $\delta^{34}S$ values of sphalerite, galena, and sulfosalts range from –1.8 to +4.1‰, –0.4 to –7.9 ‰, and –4.9 to –6.1‰. $\delta^{34}S$ values of stibnite from the stibnite–quartz veins vary from –10.0 to +0.8‰.

$\delta^{34}S_{H_2S}$ values of the fluid equilibrated with sulfide minerals at their deposition were calculated using equations of the isotope fractionation (Ohmoto and Rye, 1979):

$$\Delta_{\text{pyrite}-H_2S} = 1000\ln\alpha = \delta^{34}S_{\text{pyrite}} - \delta^{34}S_{H_2S} = 0.4(10^6/T^2), \quad (1)$$

$$\Delta_{\text{galena}-H_2S} = 1000\ln\alpha = \delta^{34}S_{\text{galena}} - \delta^{34}S_{H_2S} = -0.63(10^6/T^2), \quad (2)$$

$$\Delta_{\text{sphalerite}-H_2S} = 1000\ln\alpha = \delta^{34}S_{\text{sphalerite}} - \delta^{34}S_{H_2S} = 0.1(10^6/T^2). \quad (3)$$

$\delta^{34}S_{H_2S}$ values of the fluid that deposited sulfosalts were calculated assuming that fractionation of isotopes between these minerals and the fluid could be approximately described by the equation of fractionation between stibnite and H_2S.

$\delta^{34}S_{H_2S}$ values equal to –3.9 to –9.9‰ (an average $\delta^{34}S_{H_2S}$ is –7.0‰) were obtained for the fluid that deposited pyrite I and arsenopyrite I of the auriferous sulfide megastage at 350°C (Fig. 11b). Assuming that the deposition of sulfides at the rare metal megastage occurred at different temperatures, $\delta^{34}S_{H_2S}$ values of the fluid that deposited pyrite II were calculated for 350°C, and those for sphalerite and galena, for 250°C. They range from –0.1 to –3.1‰, –1.4 to +3.8‰ (on average, $\delta^{34}S_{H_2S}$ is +1.6‰), and –5.6 to +1.9‰ (on average, $\delta^{34}S_{H_2S}$ is +0.8‰), respectively. $\delta^{34}S_{H_2S}$ values of –0.7 to –1.8‰ were obtained for the fluid responsible for the crystallization of sulfosalts. Thus, in general, the $\delta^{34}S_{H_2S}$ values in the fluid that deposited sulfides at the rare metal megastage can be estimated as equal to 0 ± 3‰. $\delta^{34}S_{H_2S}$ values in the fluid equilibrated with stibnite at 150°C range from –5.7 to +5.0‰ (the average value is –1.0‰).

GENETIC CHARACTERISTICS OF THE DEPOSIT

Data on time relationships among mineral aggregates, mineral compositions of ores, chemical compositions of minerals, fluid inclusion compositions, and the stable isotope ratios in minerals allow us to conclude that commercial significance such as commercial disseminated auriferous sulfide, noncommercial cassiterite–sulfide, and insignificant gold–stibnite ores occur at the Maiskoe deposit. The disseminated auriferous sulfide ores are the oldest ones. They formed in an environment of tectonic compression. The rare metal mineralization deposited after the disseminated ores. The formation of the deposit was completed with the crystallization of the quartz–stibnite veins. The two last mineralization styles crystallized in open space fractures.

Fluid Regime, Fluid Sources, and Formation Conditions

The study of fluid inclusions revealed that the mineral deposition developed in the Maiskoe ore-forming system from fluids with contrasting chemical compositions. The superposition of mineral aggregates of different megastages in the same mineralized zones and findings of fluid inclusions of different types in quartz from a single sample make it difficult to determine the relative age of primary fluid inclusions. Fluid inclusions of types 1 and 2 are generally observed in quartz from the quartz–wolframite and quartz–cassiterite–sulfide assemblages. Fluid inclusions of types 4 and 5 are most common in quartz from the quartz–stibnite veins, although they occur in quartz of the stannite–sphalerite assemblage as well. Fluid inclusions of types 3 and 4 are observed in quartz from different assemblages. It is possible that fluid inclusions of the same type in quartz of different generations were found because the later inclusions were trapped by quartz on its recrystallization.

Disseminated ores of the auriferous sulfide megastage deposited when two immiscible fluids with contrasting phase compositions simultaneously coexisted in the mineral-forming system. The first fluid was a liquid low to moderate saline H_2O–CO_2 fluid with a CH_4 admixture, while the second was vapor-rich and mainly consisted of CO_2 with insignificant amounts of H_2O and CH_4. The carbon dioxide and methane content in fluid ranged from 1.6–5.2 and 0.6–1.6 mol/kg of solution, respectively. These fluids could originate as a result of phase separation of a fluid that was a H_2O–CO_2–CH_4–NaCl mixture on a temperature decrease or pressure drop. As minerals crystallized from the immiscible fluids, the homogenization temperatures of fluid inclusions can be accepted as the mineral formation temperatures. Thus, the disseminated ores were deposited at 430–238°C. The occurrence of syngenetic liquid-rich and vapor-rich fluid inclusions allows us to calculate the fluid pressure at the intersection of the isotherm in the H_2O–CO_2 system (the homogenization temperature of type 3 fluid inclusions) and the isochors,

the position of which was determined from the study of vapor-rich fluid inclusions of type 4. Pressure was found to range from 1240 to 190 bars. This assumes that the maximal depth of the ore deposition reached 3 km if it occurred at the lithostatic pressure.

The $\delta^{18}O$ value of H_2O in the fluid that deposited quartz I was calculated based on the oxygen isotope compositions of this mineral. $\delta^{34}S_{\Sigma S}$ in the mineral-forming fluid was estimated based on sulfur isotope compositions of pyrite I. Assuming that these minerals deposited at 350°C, the $\delta^{18}O_{H_2O}$ and $\delta^{34}S_{\Sigma S}$ values were estimated as $+8 \pm 1.5‰$ and $-2 \pm 2‰$ (Bortnikov *et al.*, 2003). This assumes the involvement of magmatic water ($\delta^{18}O$ is between +5.5 and +9.5‰) and sulfur ($\delta^{34}S_{\Sigma S}$ is between –3.0 and +7.0‰) (Ohmoto, 1986) in the mineral formation.

Cassiterite–sulfide mineralization of the second megastage formed under diverse geological, tectonic, and physicochemical conditions. As the predominant morphology of orebodies is the open space-filling veins, it can be concluded that the compression environment, in which early disseminated ores were formed, was replaced by an extension environment. The fluid inclusion study showed that rare metal mineralization deposited from highly concentrated H_2O–CO_2 fluids. As the mineral formation occurred from fluids that did not undergo phase separation, the determination of the true temperature of the mineral formation requires a correction of the homogenization temperature of fluid inclusions. These values can be considered as the minimal temperatures of deposition. Thus, the quartz–wolframite mineral assemblage formed at the temperatures above 500°C.

The deposition of the sulfide mineral assemblages occurred at lower temperatures. Fluid inclusions in quartz associated with pyrrhotite and chalcopyrite were homogenized at 316–333°C. The sphalerite–stannite geothermometer permitted us to estimate the formation temperatures of the stannite–sphalerite assemblage present in different ore veins and range them from 200 to 300°C. The homogenization temperatures of fluid inclusions in quartz from the same assemblage, equal to 223–170°C, indicate that the deposition of these mineral assemblages of the rare metal megastage was completed at temperatures of about 200°C. It should be noted that the rare metal mineralization was superimposed at higher temperatures than the early disseminated auriferous sulfide mineralization. The deposition of mineral assemblages of this megastage occurred as a result of a decrease in both temperature and oxidation state. The early cassiterite–pyrite–arsenopyrite mineral assemblage formed in an oxidation environment and at relatively high temperatures, while, based on experimental data (Nekrasov, 1976; Osadchii and Sorokin, 1989), the stannite–sphalerite assemblage was deposited under reduced or moderate oxidation conditions at higher sulfur fugacity ($f_{S_2} = 10^{-2}$–10^{-22} bars) and low oxygen fugacity ($f_{S_2} = 10^{-30}$ bars), assuming a crystallization temperature of 300°C.

The sulfide mineralization of the rare metal megastage, at least partially, was deposited from the immiscible fluid. This conclusion is evidenced by the finding of syngenetic fluid inclusions of types 4 and 5 in quartz from the assemblage of the Bi and Te minerals with pyrrhotite. This assemblage crystallized from an aqueous fluid with salinity of 4.8 wt % NaCl-equiv. and a vapor-rich fluid, which originated, probably, due to phase separation of the fluid on a temperature decrease or pressure drop. At the same time, the sulfide ores were deposited from low saline (5.0–5.3 wt % NaCl-equiv.) and highly saline fluids. This conclusion was confirmed by fluid inclusions with salinity of 30.2 wt % NaCl-equiv. trapped by quartz associated with stannite and sphalerite.

The occurrence of coexisting syngenetic H_2O-rich and vapor-rich fluid inclusions in quartz from the Bi and Te mineral assemblage with pyrrhotite gave us an opportunity to estimate the fluid pressure of the deposition of this assemblage. It was equal to 405–450 bars. Under lithostatic pressure, these ores formed at a depth of about 1.2 km.

The $\delta^{18}O_{H_2O}$ value in the fluid that deposited the cassiterite–sulfide mineralization of the rare metal megastage was calculated using the results of the oxygen isotope ratio study in quartz II assuming that isotope equilibrium between the fluid and quartz was attained and the average depositional temperature of this quartz was 400°C. The data obtained lie in the range of +2.3 to +10.4‰. These data assume mixing of fluids derived from different sources. The isotopically light fluid could originate on heating of meteoric water penetrating deep levels, while the fluid enriched in the heavy oxygen isotope was magmatic in origin.

The $\delta^{34}S_{\Sigma S}$ value in the fluid that deposited both pyrite and arsenopyrite and sphalerite was calculated at 300°C and 250°C, respectively, because it was previously shown that the deposition of sphalerite and stannite occurred at 200–300°C, while early arsenopyrite and pyrite were precipitated at higher temperatures. The $\delta^{34}S_{\Sigma S}$ values of the mineral-forming fluid that deposited later galena and sulfosalts were calculated assuming their crystallization at lower temperatures such as 150°C. The data obtained lie in the range of –9.9 to –3.4‰. These isotopic ratios are characteristic for sulfur of sedimentary rocks (Ohmoto, 1986). This data suggests that sulfur leached from country rocks could play an important role in the composition of the mineral-forming fluid of the rare metal megastage.

Quartz–stibnite veins of the gold–stibnite megastage formed mainly from the aqueous fluid with salinity from 0.7 to 10.1 wt % NaCl-equiv. at 120–230°C. $\delta^{18}O_{H_2O}$ in the fluid that deposited quartz of the quartz–stibnite veins was calculated using the oxygen isotope

compositions of this mineral assuming that this mineral crystallized in equilibrium with the fluid at 200°C. These values lie in the range of –5.1 to +3.5‰. They are typical for meteoric water (Ohmoto, 1986). This suggests that the mineral-forming fluid originated on heating of meteoric water and its interaction with country rocks. The $\delta^{34}S_{\Sigma S}$ values in the mineral-forming fluid that deposited stibnite range from –5.8 to +5.0‰. These values indicate that sulfur from a magma chamber and sulfur leached from country rocks were involved in the mineral formation.

Thus, a rather complicated fluid regime of the deposition of the different ores is one of the most interesting features of the Maiskoe deposit. The fluid that was a H_2O–CO_2–CH_4–NaCl mixture with salinity of 2.0–8.0 wt % NaCl-equiv. was involved into the mineral-forming system at the auriferous sulfide megastage. This fluid underwent immiscibility and was transformed into two fluids at temperatures of 430–240°C and pressures of 400–1200 bars. One of them was the H_2O–CO_2 fluid, while the second one was the vapor-rich fluid mainly consisting of carbon dioxide. It seems probable that this process caused the deposition of the disseminated sulfide ores. The escape of volatile components such as CO_2, CH_4, H_2S, H_2, and HN_3 at the phase separation resulted in oxidation and a pH increase of the residual H_2O–CO_2 fluid. As a result, this disequilibrated fluid interacted with minerals of the surrounding rocks (Bortnikov *et al.*, 1998). This led to the formation of thick halos of quartz–sericite–carbonate rocks with disseminated sulfides.

Reactions such as

$$KAl_3Si_3O_{10}(OH)_{2(\text{sericite})} + 3SiO_{2(\text{quartz})} + 8FeAsS_{(\text{arsenopyrite})} + 24H_2O + 6O_2 = KFe_3AlSi_3O_{10}(OH)_{2(\text{biotite})} + Fe_5Al_2Si_3O_{10}(OH)_{8(\text{chlorite})} + 8H_3AsO_3^0 + 8H_2S^0$$

and

$$4KAl_3Si_3O_{10}(OH)_{2(\text{sericite})} + 12SiO_{2(\text{quartz})} + 20FeAsS_{(\text{arsenopyrite})} + 62H_2O + 15O_2 = 4KAlSi_3O_{8(\text{K-feldspar})} + 4Fe_5Al_2Si_3O_{10}(OH)_{8(\text{chlorite})} + 20H_3AsO_3^0 + 20H_2S$$

led to the formation of arsenopyrite on the sulfidation of the Fe^{2+} ion contained in the silicate minerals from country rocks. The deposition of abundant sulfides such as arsenopyrite and pyrite decreased H_2S content in the mineral-forming fluid, which led in turn to the destabilization of the bisulfide complex of gold, which transported this metal in low saline fluids. The absence of native gold crystallized simultaneously with pyrite in altered wall rocks suggests that the mineral-forming fluids were undersaturated in relation to metallic gold. Possibly, this metal could be incorporated in arsenopyrite and to a lesser degree in pyrite as "chemically bound gold" (Genkin *et al.*, 1998). Thermodynamic calculations showed that the sulfide (pyrite) ores containing about 3 g/t Au are deposited at 250–400°C from fluids undersaturated by 0.5–1.5 orders of the concentration of this metal dissolved in fluids equilibrated with metallic gold (Bortnikov *et al.*, 2003). Under these conditions, electrochemical reactions occurring at contacts of sulfide grains evidently cause the crystallization of gold. Experimental studies (Jean and Bancroft, 1985) have demonstrated the role of the electrochemical phenomenon in the deposition of gold. These authors suggested a two-stage mechanism of the gold crystallization. At first, monovalent gold migrating in a fluid as chlorine or bisulfide complexes is adsorbed on the surface of grains by the sulfide group that occurs in the crystal structure of these minerals. Then, the reduction of Au^+ to Au^0 proceeds. Reactions describing these phenomena are as follows:

$$Au(HS)_2^- + S^{-2} + 12H_2O = Au^0_{\text{solid}} + 3HSO_4^- + 23H$$

if gold is transported as bisulfide complexes.

It should be emphasized that the formation of so-called orogenic deposits (Groves *et al.*, 2003) occurred from the fluid that was a H_2O–CO_2–CH_4–NaCl mixture at the physicochemical parameters at which the disseminated ores at the Maiskoe deposits have been formed as well. Many researchers believe that fluid of this composition is generated during regional metamorphism on the devolatilization and decarbonatization of rocks. Evidence for the involvement in their formation of the H_2O–CO_2 magmatic fluid was found during study of several deposits (Bortnikov *et al.*, 1996, 1997, 1998, 1999, 2001). Data on the oxygen isotope compositions of the fluid that deposited the auriferous sulfide ores at the Maiskoe deposit indicate the magmatic origin of the mineral-forming fluid, although the values obtained do not permit us to rule out participation of the metamorphic fluid as well.

The fluid regime at which the deposition of the mineralization of the rare metal megastage occurred seems to be extremely variable. It differed from the fluid regime during formation of the disseminated auriferous sulfide mineralization. The fluid inclusion study showed that the deposition of early minerals occurred from high-temperature brines, although the sulfide ores formed from moderate-temperature and saline fluid that coexisted with the vapor-rich fluid. The involvement of relatively low-temperature brines was established. Fluids with such contrasting salinity and temperatures inflowed, probably, from different sources than those that deposited early ores. Moreover, a question arises whether the change of salinity and temperatures of the fluids of the rare metal megastage was a result of the evolution of the same fluid or fluids derived from different sources participated in the ore formation. It is known that brines can originate on the evolution of the fluid exsolved at granite magma crystallization. In this case, the separation of the single-phase subcritical fluid

with moderate (~8 wt % NaCl-equiv.) salt content or the high-density liquid H_2O–NaCl phase and low saline vapor-rich phase occurs (Burnham, 1979; Fournier, 1987). The low saline vapor-rich phase and highly saline fluid (up to 55 wt % NaCl-equiv.) originate on the phase separation of the low saline fluid (Henley and McNabb, 1978; Sinohara and Hedenquist, 1997). A simultaneous circulation of both low saline fluids and brines in the magmatic–hydrothermal systems is considered to evidence an immiscibility of the initial moderate saline fluid or a direct exsolution of brines and vapor phase from the solidified magma at low pressures (Bodnar *et al.*, 1995). As no syngenetic fluid inclusions that trapped both low saline solutions and brines were observed in quartz deposited at the rare metal megastage and their homogenization temperatures are different, the phase separation should be ruled out. During the formation of late sulfide ores, fluids evidently originated in a different way could be involved in the mineral-forming system. This assumption is in agreement with results of the stable isotope study in quartz. The $\delta^{18}O_{H_2O}$ value in fluids, ranging from +2.5 to +9.2‰, infers the mixing of magmatic fluid and fluid formed on the transformation of heated meteoric water.

The oxygen isotope compositions of the low saline aqueous fluid, ranging from –5.1 to +3.5‰, indicate that heated meteoric water was predominant in the composition of the fluid involved into this mineral-forming system.

Formation History of the Deposit

One of the main questions that arises in the light of the above data is whether the fluids involved in the formation of the Maiskoe deposit were related to a single geological event or these contrasting fluids originated under different geological conditions. We assume that the different types of ores found at the Maiskoe deposit were formed in different geodynamic environments. This conclusion is evidenced by the change of tectonic environments and the depth of ore deposition. Mesoabyssal (up to 3 km) conditions were replaced by near-facial (1 km) environments and then shallow conditions (0.5 km) during the formation of the Maiskoe deposit.

Characteristics of the orogenic gold deposits that are formed along the active margin upon accretion or collision of terranes and are related to the plate subduction or lithosphere layering (Groves *et al.*, 1998) are typical of the disseminated auriferous sulfide deposits. Orogenic gold deposits are commonly formed during final stages of the tectonic–magmatic–metamorphic history of orogen development (Groves *et al.*, 2000, 2003). Zonenshain *et al.* (1990) showed that the dislocation of terrigenous rocks of the Chukotka territory and the injection of granite bodies occurred in the Aptian Age (115 Ma ago). As a result of the approach of the Kula plate to the Eastern Asian margin and the Chukotka territory, the Yuzhno-Anyuisk zone originated. The Chukotsk block experienced right-lateral displacement relative to Siberia under the confined compression in the Albian Age (100 Ma ago). Collision of Chukotka and Siberia with blocks inside the Kolyma plate continued at this time. Deep-seated northwest-trending sutures and injection of small intrusions of the gabbro-diorite series occurred in a compressional environment during this period. In zones of tectonomagmatic activization, terrigenous rocks were metamorphosed under conditions of the greenschist facies. Possibly, the fluids represented by the H_2O–CO_2–CH_4–NaCl mixture with salinity of 2–8 wt % NaCl-equiv. occurred upon the metamorphism of rocks as a result of their dehydration and decarbonatization. These fluids could interact with a large volume of country rocks containing disseminated digenetic sulfides, dissolve them, and then redeposit within tectonic zones due to reactions with carbonaceous rocks. The disseminated arsenic-bearing pyrite and gold-bearing arsenopyrite were, possibly, deposited at the Maiskoe deposit. Country rocks experienced the quartz–sericite and quartz–carbonate–sericite facies of the quartz–sericite–carbonate–pyrite ("beresite") alteration. As a result of the collision of Chukotka and Siberia, granitoids were injected into fold structures of Chukotka (Zonenshain *et al.*, 1990). It should be noted that the gold–quartz mineralization of Chukotka is paragenetically related to Early Cretaceous granitoid complexes. The age of this mineralization is 121–98 Ma, which coincides with the age of granitoids located inside metamorphic cupolas (Goryachev *et al.*, 1994). The mineral-forming fluids could be related to these granitoids.

Volkov and Sidorov (2001) suggested a model for the formation of the disseminated ores at the Maiskoe deposit that assumed the generation of the mineral-forming fluids by the injection of Early Cretaceous granitoids. However, these authors believed that the ore formation occurred at the accretion megastage.

A.A. Sidorov suggested that the disseminated sulfide ores at the Maiskoe deposit display characteristics similar to those of the Carlin-type deposits. We believe that the conditions of formation of the typical Carlin-type deposits (Empso *et al.*, 2003) and those of the disseminated mineralization at the Maiskoe deposit are different. These differences are as follows: (1) the Carlin-type deposits originated in an extension environment, while the ores of the Maiskoe deposit were formed under compressional conditions; (2) argillization, decarbonatization, and silicification are typical wall rock alterations at the Carlin-type deposits, while quartz–sericite–carbonate rocks ("beresites") are developed at the Maiskoe deposit; (3) the deposition of the Carlin ores occurred at relatively low temperatures of 200 ± 50°C, while the ores at the Maiskoe deposit are of higher temperatures, 350–250°C; (4) realgar and orpiment, which are typical minerals at the Carlin-type deposits, were not found at the Maiskoe deposit.

The mineralization of the rare metal megastage, possibly, is similar to the cassiterite–sulfide ores of the Kukeneisk deposit, which are paragenetically related to granitoids of the Kukeneisk massif. As their petrochemical characteristics are similar to those of tin-bearing granitoids located in many regions of the world, the paragenetic relation of the cassiterite–sulfide mineralization of the Maiskoe deposit to the granitoid magmatism may be inferred. The age of this mineralization is not older than Late Cretaceous, as ore veins cut siliceous subvolcanic dikes whose K–Ar age is 115–97 Ma (Sidorov and Volkov, 2001). The mineral formation at the Kukeneisk deposit occurred under conditions similar to those found for the cassiterite–sulfide mineralization of the Maiskoe deposit. The temperatures and salinity of fluids that deposited the Kukeneisk ores are as high as 500°C and 47 wt % NaCl-equiv. (Goncharov *et al.*, 1990). The formation of the cassiterite–sulfide ore is suggested to be related to the development of the Andean-type Okhotsk–Chukotsk active margin. In the Cordilleras, the formation of tin–tungsten deposits occurred within the island arcs and was related to the subduction that resulted in the origin of S-granites (Sillitoe, 1981).

The gold–stibnite ores at the Maiskoe deposit were formed in a near-surface environment from meteoric fluids and, probably, are similar to the stibnite veins at the weakly eroded Sopka Rudnaya occurrence located within terrigenous rocks in the Maiskoe ore field. This occurrence, situated 12 km east–southeast of the Maiskoe deposit, is considered to be the low level of the shallow volcanogenous Au–Ag ores in the Okhotsk–Chukotsk volcanoplutonic belt (Volkov and Sidorov, 2001). The quartz–stibnite veins of Sopka Rudnaya, as well as the gold–stibnite ores of the Maiskoe deposit, formed at temperatures of 230–120°C and a depth less than 0.5 km estimated at a fluid pressure below 0.2 kbar. As quartz–stibnite veins crosscut the andesite–basalt dikes that completed the magmatic activity in the Okhotsk–Chukotsk belt, the age of the quartz–stibnite veins is estimated as Late Cretaceous (Volkov and Sidorov, 2001). Goryachev (1997) showed that volcanogenous Au–Ag deposits and occurrences in the Okhotsk–Chukotsk belt formed 80–70 Ma ago. The Ar–Ar age of alular from the Valunistoe deposit (Chukotka), equal to 71.8 ± 0.2 Ma, shows that it is the youngest one in this belt.

Thus, three genetically different mineralizations of different age have been superposed at the Maiskoe deposit. These mineralizations formed in various geological and tectonic environments under different physicochemical conditions from fluids ascending from different sources. The superposition of mesoabyssal and shallow ores on the same hypsometric level suggests a time interruption between the formation of mineralizations of the disseminated auriferous sulfide and rare metal megastages. The formation of the deposit can be supposed to have occurred in the Late Cretaceous from 120 to 70 Ma. Therefore, the Maiskoe deposit is a typical example of a multicomponent polychronous and polygenic deposit.

ACKNOWLEDGMENTS

The study was supported by the Russian Foundation for Basic Research (project no. 02-05-65183) and by the Russian Academy of Sciences in the framework of the Program No. 2 of the Division of Earth Sciences, "Large and Superlarge Deposits of Strategic Mineral Resources: Geological Characteristics, Formation Conditions, and Basic Problems of Their Complex Mining and Rational Processing."

REFERENCES

1. F. P. Bierlein and S. Maher, "Orogenic Disseminated Gold in Phanerozoic Fold Belts–Examples from Victoria, Australia and Elsewhere," Ore Geol. Rev. **17**, 215–232 (2001).
2. R. J. Bodnar and M. O. Vityk, "Interpretation of Microthermometric Data for H_2O–NaCl Fluid Inclusions," in *Fluid Inclusions in Minerals: Methods and Applications* (Pontignano-Siena, 1994), pp. 117–130.
3. R. J. Bodnar, C. W. Burnham, and S. M. Sterne, "Synthetic Fluid Inclusions in Natural Quartz. III. Determination of Phase Equilibrium Properties in the System H_2O–NaCl to 1000°C and 1500 Bars," Geochim. Cosmochim. Acta **49**, 1861–1873 (1995).
4. A. S. Borisenko, "Study of Salt Composition of Fluid Inclusions in Minerals by Cryometric Technique," Geol. Geophys., No. 8, 16–27 (1977) [in Russian].
5. N. S. Bortnikov, V. Yu. Prokof'ev, and N. V. Razdolina, "Origin of the Charmitan Gold–Quartz Deposit (Uzbekistan)," Geol. Rudn. Mestorozhd. **38** (3), 238–257 (1996) [Geol. Ore Deposits **38** (3), 47–65 (1996)].
6. N. S. Bortnikov, L. Cabri, I. V. Vikentiev, *et al.*, "Invisible Gold in Sulfides from Seafloor Massive Sulfide Edifices", Geol. Rudn. Mestorozhd. **45** (3), 228–240 (2003) [Geol. Ore Deposits **45** (3), 201–212 (2003)].
7. N. S. Bortnikov, V. V. Murzin, V. N. Sazonov, *et al.*, "The Svetlinsk Gold–Telluride Deposit, Urals, Russia: Mineral Paragenesis, Fluid Inclusion and Stable Isotope Studies," in *Mineral Deposits: Processes to Processing* (Balkema, Rotterdam, 1999), Vol. 1, pp. 21–28.
8. N. S. Bortnikov, G. N. Gamyanin, V. V. Alpatov, *et al.*, "Mineralogy, Geochemistry and Origin of the Nezhdaninsk Gold Deposit (Sakha-Yakutia, Russia)," Geol. Rudn. Mestorozhd. **40** (2), 137–156 (1998) [Geol. Ore Deposits **40** (2), 121–156 (1998)].
9. N. S. Bortnikov, V. Yu. Prokof'ev, O. V. Vikentieva, *et al.*, "The Maiskoe Disseminated Gold Deposit, Chukotka, Russia: Mineral Paragenesis, Fluid Inclusion, Oxygen and Sulfur Isotope Studies," in *Mineral Exploration and Sustainable Development* (Millpress, Rotterdam, 2003), pp. 743–746.
10. N. S. Bortnikov, V. N. Sazonov, I. V. Vikent'ev, *et al.*, "The Berezovsk Giant Gold Quartz Deposit, Urals, Russia: Fluid Inclusion and Stable Isotope Studies," in *Mineral Deposits: Research and Exploration—Where Do They Meet?* (Balkema, Rotterdam, 1997), pp. 157–160.
11. N. S. Bortnikov, O. V. Vikentyeva, A. Fallick, and V. N. Sazonov, "REE and Y Distribution and O and D Isotope Study of Minerals from Listvenites at the Berezovsk Giant Mesothermal Gold Lode Deposit, Urals, Russia:

Evidence for Contribution of Magmatic Fluid," in *Mineral Deposits at the Beginning of the 21st Century* (Balkema, Rotterdam, 2001), pp. 707–710.

12. C. W. Burnham, "Magmas and Hydrothermal Fluids," in *Geochemistry of Hydrothermal Ore Deposit*, Ed. by H. Barnes (Wiley, New York, 1979), pp. 71–136.
13. V. A. Buryak, I. S. Nenenman, N. V. Berdnikov, *et al.*, "Fluid Regime of Formation and Source of Mineral-forming Fluids of Gold Quartz Veins of Allakh-Yun'skaya Zone," Tikhookeansk. Geol., No. 3, 62–70 (1990) [in Russian].
14. G. M. Claypool and J. R. Kaplan, "The Origin and Distribution of Methane in Marine Sediments," in *Natural Gases in Marine Sediments* (Plenum Press, New York, London, 1974), Vol. 3, p. 132.
15. R. N. Clayton, J. R. O'Neil, and T. K. Mayeda, "Oxygen Isotope Exchange between Quartz and Water," J. Geophys. Res. **77**, 3057–3067 (1972).
16. P. L. P. Collins, "Gas Hydrates in CO_2-bearing Fluid Inclusions and the Use of Freezing Data for Estimation of Salinity," Econ. Geol. **74**, 1435–1444 (1979).
17. R. S. Darling, "An Extended Equation to Calculate NaCl Contents from Final Clathrate Melting Temperatures in H_2O–CO_2–NaCl Fluid Inclusions: Implications for *P–T*-Isochors Location," Geochim. Cosmochim. Acta **55**, 3869–3871 (1991).
18. P. Empso, A. F. Hofstra, E. A. Lauha, *et al.*, "Origin of High-grade Gold Ore, Source of Ore Fluid Components, and Genesis of the Meikle and Neighboring Carlin-Type Deposits, Northern Carlin Trend, Nevada," Econ. Geol. **98**, 1069–1105 (2003).
19. M. E. Fleet and A. H. Mumin, "Gold-bearing Arsenian Pyrite and Marcasite from Carlin Trend Gold Deposits and Laboratory Synthesis," Amer. Mineral. **82**, 182–193 (1997).
20. M. E. Fleet, S. L. Chryssoulis, P. J. MacLean, *et al.*, "Arsenian Pyrite from Gold Deposits: Au and As Distribution Investigated by SIMS and EP, and Color Scanning and Surface Oxidation by XPS and LIMS," Can. Mineral. **31**, 1–17 (1993).
21. R. O. Fournier, "Conceptual Models of Brine Evolution in Magmatic–Hydrothermal Systems," US Geol. Surv. Prof. Paper **1350**, 1487–1506 (1987).
22. A. D. Genkin, N. S. Bortnikov, L. J. Cabri, *et al.*, "A Multidisciplinary Study of Invisible Gold in Arsenopyrite from Four Mesothermal Gold Deposits in Siberia, Russian Federation," Econ. Geol. **93**, 463–487 (1998).
23. A. M. Gavrilov, A. P. Pleshakov, P. S. Bernstein, *et al.*, "Submicroscopic Gold in Sulfides in Disseminated Ores of Some Deposits," Sov. Geol., No. 8, 81–86 (1982) [in Russian].
24. M. L. Gel'man, "Verkhoyansk–Chukotsk Fold Belt," in *Metamorphic Complexes of Asia* (Nauka, Novosibirsk, 1977), pp. 246–253 [in Russian].
25. R. J. Goldfarb, D. L. Leach, S. C. Rose, and G. P. Landis, "Fluid Inclusion Geochemistry of Gold-bearing Quartz Veins of the Juneau Gold Belt, Southeastern Alaska: Implications for Ore Genesis," in *Econ. Geol. Monograph* (Soc. Econ. Geol., Cero de Pasco, 1989), Vol. 6, pp. 363–375.
26. V. I. Goncharov, *Hydrothermal Ore Formation in Marginal Volcanic Belts* (Nauka, Moscow, 1983) [in Russian].
27. V. I. Goncharov, V. A. Volkov, *et al.*, "Kukeneisk Intrusion–Cupola Structure and Its Mineralization," in *Ore–Magmatic Systems of Northeast of the USSR* (Khabarovsk, 1990), pp. 115–124 [in Russian].
28. N. A. Goryachev, "Gold Mineralization and Granite–Metamorphic Cupola of Phanerozoic Fold Belts of Asia", in *Magmatism and Ore Mineralization of Northeastern Asia* (SVKNII DVO RAN, Magadan, 1997), pp. 258–273 [in Russian].
29. N. A. Goryachev, *Geology of Mesozoic Gold Quartz Vein Belts of Northeastern Asia* (SVKNII DVO RAN, Magadan, 1998) [in Russian].
30. N. A. Goryachev, N. E. Savva, and A. A. Sidorov, "Gold," in *Essays of Metallogeny and Geology of Northeast of Russia* (SVKNII DVO RAN, Magadan, 1994), pp. 22–55 [in Russian].
31. D. I. Groves, R. J. Goldfarb, F. Robert, and C. J. R. Hart, "Gold Deposits in Metamorphic Belts: Overview of Current Understanding, Outstanding Problems, Future Research, and Exploration Significance," Econ. Geol. **98**, 1–29 (2003).
32. D. I. Groves, R. J. Goldfarb, M. Gebre-Mariam, *et al.*, "Orogenic Gold Deposits: A Proposed Classification in the Context of Their Crustal Distribution and Relationship to Other Gold Deposit Types," Ore Geol. Rev. **13**, 7–27 (1998).
33. D. I. Groves, R. J. Goldfarb, C. M. Knox-Robinson, *et al.*, "Late-Kinematic Timing of Orogenic Gold Deposits and Significance for Computer-based Exploration Techniques with Emphasis on the Yilgarn Block, Western Australia," Ore Geol. Rev. **17**, 1–38 (2000).
34. R. W. Henley and A. McNabb, "Magmatic Vapor Plumes and Ground Water Interactions in Porphyry Copper Emplacement," Econ. Geol. **73**, 1–20 (1978).
35. C. J. Hodgson, D. A. Love, and J. V. Hamilton, "Giant Mesothermal Gold Deposits: Descriptive Characteristics, Genetic Models and Exploration Selection Criteria," in *Giant Ore Deposits* (Soc. Econ. Geol. Inc., Cero de Pasco, 1993), SP-2, pp. 157–206.
36. S. H. Karup-Möller, "Mineralogy of Some Ag–(Cu)–Pb–Bi Sulfide Associations," Bull. Geol. Soc. Denm. **26**, 41–68 (1977).
37. V. A. Kalyuzhnyi, *Principles of Doctrine on Mineral-forming Fluids* (Naukova Dumka, Kiev, 1982) [in Russian].
38. M. M. Konstantinov, E. M. Nekrasov, A. A. Sidorov, and S. F. Struzhkov, *Gold Giants of Russia and the World* (Nauchnyi Mir, Moscow, 2000) [in Russian].
39. N. K. Kurbanov, Ch. Kh. Arifulov, P. G. Kucherevskii, *et al.*, "Geological and Genetic Models for Gold Deposits in Carbonaceous–Terrigenous Complexes," Rudy Met., No. 2, 55–69 (1994) [in Russian].
40. G. E. Jean and G. M. Bancroft, "An XPS and SEM Study of Gold Deposition at Low Temperatures on Sulfide Mineral Surfaces: Concentration of Gold by Adsorption Reduction," Geochim. Cosmochim. Acta **49**, 979–987 (1985).
41. Y. Matsuhisa, J. R. Goldsmith, and R. N. Clayton, "Oxygen Isotopic Fractionation in the System Quartz–Albite–

Anorthite–Water," Geochim. Cosmochim. Acta **43**, 1131–1140 (1979).

42. D. T. McCoy, R. J. Newberry, P. Layer, *et al.*, "Plutonic-Related Gold Deposits of Interior Alaska," in *Econ. Geol. Monograph 9* (1997), pp. 191–241.
43. O. F. Mironova, V. B. Naumov, and A. N. Salazkin, "Nitrogen in Mineral-Forming Fluids. Gas Chromatographic Determination at Fluid Inclusion Study," Geokhimiya, No. 7, 979–991 (1992) [in Russian].
44. G. V. Moralev, N. S. Bortnikov, and V. S. Malov, "Chemical Compositions of Fahlores in Relation to Formation Conditions of a Deposit," Geol. Rudn. Mestorozhd. **30** (4), 116–121 (1988) [in Russian].
45. N. N. Mozgova, *Nonstoichiometry and Homologous Series of Sulfosalts* (Nauka, Moscow, 1986) [in Russian].
46. I. Ya. Nekrasov, *Phase Relations in Tin-Bearing Systems* (Nauka, Moscow, 1976) [in Russian].
47. B. E. Nesbitt and K. Muchlenbachs, "Geology, Geochemistry and Genesis of Mesothermal Lode Gold Deposits of the Canadian Cordillera: Evidence for Ore Formation from Evolved Meteoric Water," in *Econ. Geol. Monograph 6* (1989), pp. 553–563.
48. R. J. Newberry, D. T. McCoy, and D. A. Brew, "Plutonic-Hosted Gold Ores in Alaska: Igneous vs. Metamorphic Origins," in *Resource Geology Special Issue* (1995), No. 18, pp. 57–100.
49. Yu. I. Novozhilov and A. M. Gavrilov, *Gold–Sulfide Deposits in Carbonaceous–Terrigenous Sequences* (TsNIGRI, Moscow, 1999) [in Russian].
50. Yu. I. Novozhilov, A. M. Gavrilov, and A. A. Sidorov, "Silver in Deposits of Disseminated Ores with Finely-Dispersed Gold," in *Trudy TsNIGRI* (1982), Issue 167, pp. 60–67 [in Russian].
51. H. Ohmoto, "Stable Isotope Geochemistry of Ore Deposits," in *Stable Isotopes in High Temperature Geological Processes. Rev. in Mineralogy* (1986), Vol. 16, pp. 491–560.
52. H. Ohmoto and R. O. Rye, "Isotopes of Sulfur and Carbon," in *Geochemistry of Hydrothermal Ore Deposits*, Ed. by H. Barnes (Wiley, New York, 1979), pp. 509–567.
53. E. G. Osadchii and V. I. Sorokin, *Stannite-Bearing Sulfide Systems* (Nauka, Moscow, 1989) [in Russian].
54. L. M. Parfenov, "Terranes and History of Formation of Mesozoic Orogenic Belts of Eastern Yakutia," Tikhookeansk. Geol., No. 6, 32–43 (1995) [in Russian].
55. L. M. Parfenov, L. M. Natapov, S. D. Sokolov, *et al.*, "Terranes and Accretion Tectonics of Northeast of Asia," Geotektonika, No. 1, 68–78 (1993) [in Russian].
56. N. I. Savel'eva, V. Yu. Prokof'ev, A. M. Dolgonosov, *et al.*, "Use of Ion Chromatography Technique at Study of Anion Composition of Solution in Fluid Inclusions," Geokhimiya, No. 3, 401–408 (1988) [in Russian].
57. A. A. Sidorov and A. V. Volkov, "Unique Ore District of Chukotka," Tikhookeansk. Geol., No. 4, 3–18 (2001) [in Russian].
58. A. A. Sidorov and I. N. Tomson, "Formation Conditions of Sulfidized Black Shale Sequences and Their Metallogenic Significance," Tikhookeansk. Geol. **19** (6), 83–92 (2000) [in Russian].
59. R. H. Sillitoe, "Ore Deposits in Cordilleran and Arc-Related Setting," Arizona Geol. Soc. **XIV**, 49–70 (1981).
60. H. Sinohara and J. W. Hedenquist, "Constraints on Magma Degassing beneath the Far Southeast Porphyry Cu–Au Deposit, Philippines," J. Petrol. **38**, 1741–1752 (1997).
61. N. A. Shilo, V. I. Goncharov, V. A. Al'shevskii, and V. V. Vortsepnev, *Formation Conditions of Gold Mineralization in Structures of Northeast of the USSR* (Nauka, Moscow, 1988) [in Russian].
62. N. A. Shilo, M. S. Sakharova, N. N. Krivitskaya, S. K. Ryakhovskaya, I. A. Bryzgalov, *Mineralogy and Genesis of Gold-Silver Mineralization of the Northwestern Pacific Framing* (Nauka, Moscow, 1992) [in Russian].
63. V. I. Shpikerman, *Pre-Cretaceous Minerageny of Northeast of Asia* (SVKNII DVO RAN, Magadan, 1998) [in Russian].
64. V. I. Shpikerman and N. A. Goryachev, "Plate Tectonic Metallogeny of Fold Systems of Accretion Type," in *Metallogeny of Fold Systems Based on Concept of Plate Tectonics* (Yekaterinburg, UrO RAN, 1996), pp. 64–78 [in Russian].
65. E. M. Spiridonov, "Typomorphic Features of Fahlores of Some Plutonogenic, Volcanogenic, and Telethermal Gold Deposits," Geol. Rudn. Mestorozhd. **29** (6), 83–92 (1987) [in Russian].
66. J. F. H. Thompson and R. J. Newberry, "Gold Deposits Related to Reduced Granitic Intrusions," in *Gold in 2000* (Soc. Econ. Geol. Inc., Littleton, 2000), Vol. 13, pp. 377–400.
67. I. N. Tomson, A. A. Sidorov, O. P. Polyakova, and V. P. Polokhov, "On New Type of Carbon–Ilmenite–Sulfide Mineralization of Non-Hydrothermal Origin," Dokl. Ross. Akad. Nauk **279** (3), 727–730 (1984) [in Russian].
68. A. V. Volkov, "Gold Deposits of Central Chukotka," Geol. Rudn. Mestorozhd. **37** (6), 482–499 (1995) [Geol. Ore Deposits **37** (6), 420–435 (1995)].
69. A. V. Volkov and A. A. Sidorov, *Unique Gold District of Chukotka* (SVKNII DVO RAN, Magadan; IGEM RAN, Moscow, 2001) [in Russian].
70. L. P. Zonenshain, M. I. Kuz'min, and L. M. Natapov, *Tectonics of Lithospheric Plates of the USSR Territory* (Nedra, Moscow, 1990) [in Russian].

View publication stats